Solar Phys (2017) 292:138
DOI 10.1007/s11207-017-1162-8

Initial Results from Fitting *p*-Modes Using Intensity Observations from the *Helioseismic and Magnetic Imager*

Sylvain G. Korzennik[1]

Received: 12 May 2017 / Accepted: 23 August 2017 / Published online: 12 September 2017

Abstract The *Helioseismic and Magnetic Imager* project recently started processing the continuum-intensity images following global helioseismology procedures similar to those used to process the velocity images. The spatial decomposition of these images has produced time series of spherical harmonic coefficients for degrees up to $\ell = 300$, using a different apodization than the one used for velocity observations. The first 360 days of observations were processed and are made available. I present initial results from fitting these time series using my fitting method and compare the derived mode characteristics to those estimated using coeval velocity observations.

Keywords Sun: oscillations · Sun: helioseismology

1. Introduction

Recently, the *Helioseismic and Magnetic Imager* (HMI: Schou *et al.*, 2012) project started processing the HMI continuum-intensity images following procedures similar to those used to process the *Michelson Doppler Imager* (MDI) and the HMI velocity images. This generated time series of spherical harmonic coefficients suitable for global helioseismology mode fitting.

The spatial decomposition of apodized intensity images was carried out for the first 360 days of the HMI science-quality data, producing time series of spherical harmonic coefficients for degrees up to $\ell = 300$. Since the oscillatory signal in intensity is not attenuated by a line-of-sight projection, the intensity images were apodized differently from the velocity images. Moreover, since the global helioseismology data-processing pipeline was developed using velocity images, the automatic detection of discontinuities in the intensity data has yet to be implemented and validated. For this reason, the HMI project has not yet applied its gap-filling to the resulting time series.

✉ S.G. Korzennik
skorzennik@cfa.harvard.edu

[1] Harvard-Smithsonian Center for Astrophysics, Cambridge, MA 02138, USA

Global solar p-mode oscillations were detected in intensity several decades ago by Woodard (1984) with the *Active Cavity Radiometer Irradiance Monitor* (ACRIM) instrument onboard the *Solar Maximum Mission* (SMM) spacecraft, and later extensively observed with the *Variability of Solar Irradiance and Gravity Oscillations* instruments assembly (VIRGO: Froehlich *et al.*, 1988) onboard the *Solar and Heliospheric Observatory* (SOHO), which includes the three-channel *Sunphotometers* (SPM) and the *Luminosity Oscillations Imager* (LOI). Yet, the intensity images in most spatially resolved experiments are not routinely analyzed. Indeed, neither the *Global Oscillation Network Group* (GONG) nor the MDI or HMI pipelines process the intensity images.

Historically, solar oscillation data have been acquired and analyzed using intensity fluctuations for disk-integrated observations (see Frohlich *et al.*, 1997; Salabert, García, and Jiménez, 2013, for examples). For a few cases, intensity images have been reduced (Corbard *et al.*, 2013), and in most cases, a cross-spectral analysis was carried out on m-averaged spectra and without the inclusion of any spatial leakage information (Oliviero, Severino, and Straus, 2001; Barban, Hill, and Kras, 2004).

None of these studies led to a routine reduction and analysis of the intensity images, since the "noise" properties of the intensity data are quite different from the velocity data and fewer modes can be fitted. Nevertheless, fitting intensity data allows for an independent validation of the fitting methodology and further confirmation for the need to fit an asymmetric profile.

Indeed, the GONG, MDI, and HMI pipelines are still fitting symmetric profiles to mode peaks that are known to be asymmetric. Moreover, the GONG pipeline simply ignores the leakage matrix,[1] while the MDI and HMI pipeline includes the leakage matrix, but continues to routinely fit symmetric profiles.

The MDI and HMI mode-fitting procedure was retrofitted to include an asymmetry, but when using asymmetric profiles, it fits fewer modes successfully, and it produces a more inconsistent set of modes with fitted epoch. Finally, the mode asymmetry measured by the MDI and HMI fitting procedure barely changes with time or activity level, while the mode asymmetry measured with my method shows changes that correlate with the solar-activity levels (see Korzennik, 2013).

By fitting the intensity and the velocity independently, we can validate both the inclusion of the leakage matrix and the proper modeling of the asymmetry. Indeed, the intensity leakage is substantially different from the velocity leakage, and the mode frequency ought to be the same whether the oscillatory signal is observed and measured in intensity or velocity. By contrast, a cross-spectral analysis models both the intensity and the velocity spectra, but fits a single parameter for the mode frequency, hence the velocity and intensity frequency is the same by construction.

In this article I present my first attempt to fit these time series using my fitting method (Korzennik, 2005, 2008). While that method is in principle perfectly suited to velocity or intensity observations, a leakage matrix specific to intensity observations was needed.

I fitted four consecutive 72-day long time series of intensity observations as well as one 288-day long time series (*i.e.* one that was four times longer). I carried out my mode fitting using the same procedures as I use for velocity observations, although I first refined the initial guess used for the mode profile asymmetry to be appropriate for intensity observations, and I used a leakage matrix appropriate for intensity observations. I also ran my

[1] A leakage matrix is the characterization of the spatial leaks, *i.e.* the relative amplitude of the signal from adjacent ℓ and m in any target (ℓ, m) spherical harmonic coefficient, which results from the fact that one can only observe the visible fraction of the Sun while the spherical harmonic functions are orthonormal on the complete sphere.

Table 1 Length, start and end time of fitted time series, and their respective duty cycles. The duty cycles of the velocity time series correspond to the gap-filled series, and the duty cycles of the intensity time series correspond to the raw series.

Length [day]	Start time [TAI]	End time [TAI]	Duty cycle [%]	
			Velocity	Intensity
72	2010.04.30 00:00	2010.07.10 23:59	99.991	99.660
	2010.07.11 00:00	2010.09.20 23:59	99.466	98.328
	2010.09.21 00:00	2010.12.01 23:59	99.468	97.078
	2010.12.02 00:00	2011.02.11 23:59	99.462	98.958
288	2010.07.11 00:00	2011.04.24 23:59	99.366	97.774

fitting procedure by forcing the mode profile to be symmetric. Finally, in order to extend the comparison to the 288-day long time series, I ran my fitting procedure on the same co-eval 288-day long time series using the velocity observations and fitting symmetric mode profiles.

I describe in Section 1.3 the various leakage-matrix coefficient estimates that I computed and/or used, and how I tried to validate them against the observed power distribution with m. The results from fitting intensity observations are presented in Section 2, and I first compare in Section 2.4 the results obtained from fitting the same intensity-observations time series using two different leakage matrices. Section 2.5 shows comparisons between mode parameters derived from fitting intensity and velocity observations, all using my fitting methods, but also cases that were run leaving the mode profile symmetric.

1.1. Dataset

The data used for this study are time series of spherical harmonic coefficients computed by the HMI project at Stanford using the continuum intensity images taken by HMI onboard the *Solar Dynamic Observer* (SDO). This dataset is tagged at the SDO/HMI and AIA *Joint Science Operations Center* (JSOC) as hmi.lc_sht_72d. Four consecutive time series, each 72 days long, were produced for degrees up to $\ell = 300$ and for all azimuthal orders $[m]$ starting on 30 April 2010 at 00:00:00 TAI. These time series were not gap-filled, although the fill factors are high, namely between 97.078 and 99.660%. One 288-day long time series was constructed using, for consistency with previous analysis, four 72-day long time series starting on 11 July 2010 at 00:00:00 TAI (*i.e.* 72×72 days after the start of MDI science-quality data). The start and end time of the fitted time series and their respective duty cycles are listed in Table 1.

1.2. Brief Description of the Fitting Method

My fitting method is described in detail by Korzennik (2005, 2008). The first step consists of computing sine multi-taper power spectra, with the number of tapers optimized to match the anticipated observed line-width (*i.e.* the intrinsic line-width convolved by the observing window function) of the modes being fitted; hence the number of tapers is not constant for a given time-series length[2] (see Korzennik, 2005, for details). The second step consists of

[2]For 72-day long time series, the number of tapers is between 3 and 33 (*i.e.* 3, 5, 9, 17, or 33), while for the 288-day long time series it is between 3 and 129 (*i.e.* 3, 5, 9, 17, 33, 65, or 129).

simultaneously fitting all of the azimuthal orders for a given mode, using a fraction of the power spectrum centered around the fitted mode. Each singlet, *i.e.* a peak of a given (n, ℓ, m), is modeled by an asymmetric mode profile characterized by its own frequency, amplitude, and background, and by a line width and asymmetry that is the same for all azimuthal orders; hence the fitted model assumes[3] that the full width at half-maximum (FWHM) and the asymmetry are independent of m. The fitted model includes a complete leakage matrix, where the leaked modes for the same n but a different ℓ and m are attenuated by the ratio of the respective leakage-matrix components. Contamination by nearby modes, namely modes with a different n, ℓ, and m, is also included in the model when these modes are present in the spectral fitting window.

The model is fitted simultaneously, in the least-squares sense, to the observed $2\ell + 1$ multi-tapered power spectra. For numerical stability the fitting is made in stages, *i.e.* not all of the parameters are fitted simultaneously right away, and a sanity check is performed along the way: modes whose amplitude is not above some threshold based on the signal-to-noise ratio (S/N) of the spectrum are no longer fitted. A third step consists of iterating the fitting of each mode using the results of the previous iteration to account for the mode contamination.

Sections of power spectra $[P_{n,\ell,m}(\nu)]$ are modeled as

$$P_{n,\ell,m}(\nu) = \Sigma_{\ell',m'}\left(\frac{C(\ell,m;\ell',m')}{C(\ell,m;\ell,m)}A_{n,\ell',m'}\mathcal{L}(x,\alpha_{n,\ell''}) + B_{n,\ell',m'}\right) + \Sigma_{n'}P_{n',\ell,m}(\nu), \quad (1)$$

where

$$x = \frac{\nu - \nu_{n,\ell',m'}}{2\Gamma_{n,\ell'}}, \quad (2)$$

and ν is the frequency, $\mathcal{L}$ a generalized asymmetric Lorentzian, defined as

$$\mathcal{L}(x,\alpha) = \frac{1+\alpha(x-\frac{\alpha}{2})}{1+x^2}, \quad (3)$$

and $\nu_{n,\ell,m}$, $\Gamma_{n,\ell}$, $\alpha_{n,\ell}$, $A_{n,\ell,m}$, and $B_{n,\ell,m}$ are the mode frequency, FWHM, asymmetry, power amplitude, and background, respectively, while $C(\ell,m;\ell',m')$ are the leakage-matrix coefficients.

1.3. Intensity Leakage Matrix

1.3.1. Sensitivity Function and Limb Darkening

In contrast to the velocity oscillatory signal (see, for example, Korzennik, 2005), the intensity oscillatory signal is a scalar, leading to a simpler leakage matrix, namely

$$C(\ell,m;\ell',m') = \int \mathcal{A}(\mu)J(\mu)Y_\ell^{m*}(\theta,\phi)Y_{\ell'}^{m'}(\theta,\phi)\,\mathrm{d}\Omega, \quad (4)$$

where θ is the colatitude, ϕ is the longitude, μ is the fractional radius of the image of the solar disk, $\mathcal{A}$ is the apodization used in the spatial decomposition, J is the sensitivity of the oscillatory signal, Y_ℓ^m is the spherical harmonic of degree ℓ and azimuthal order m,

[3] Although this assumption is likely to be invalidated at some level by the latitudinal distribution of the solar magnetic field.

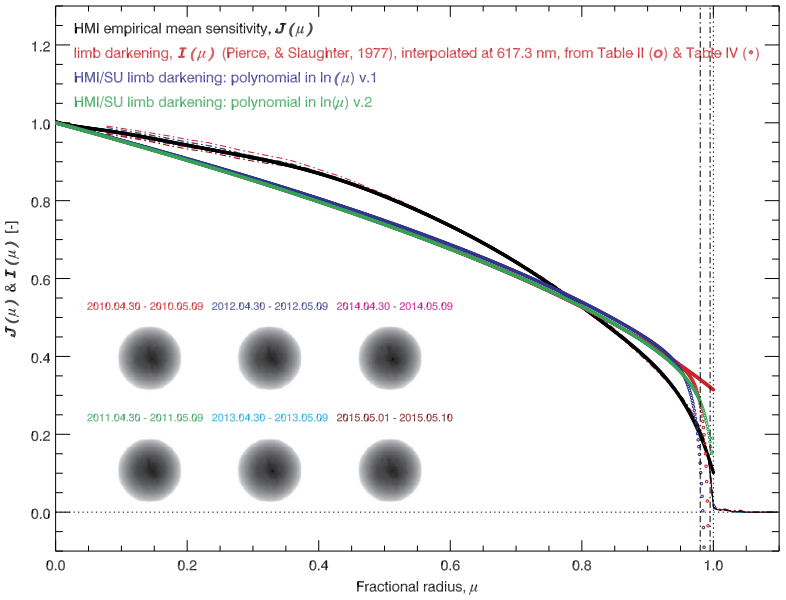

Figure 1 Empirical sensitivity functions $[J(\mu)]$ and limb-darkening functions $[I(\mu)]$ as a function of the fractional radius $[\mu]$. The *colored dashed curves* are estimates of $J(\mu)$ derived from ten days of data taken in six consecutive years. The images of the RMS of the residuals used for this derivation are shown with the corresponding color-coded time ranges. The *solid-black line* is the average of these six profiles, and the *black dots* show the corresponding polynomial fit to this average that was used for one leakage-matrix computation. The *colored dots and circles* correspond to limb-darkening profiles computed using different polynomial parametrization: Tables II and IV from Pierce and Slaughter (1977), interpolated for $\lambda = 617.3$ nm, and coefficients used by the Stanford group (T.P. Larson, 2017, private communication). *Open circles* correspond to polynomials in $x = \ln(\mu)$, *dots* to polynomials in μ. Note how the different limb-darkening representations disagree only near the limb, and that the polynomial parametrization with respect to $x = \ln(\mu)$ leads to negative values near the limb. *Vertical lines* are drawn to indicate the location of the limb and the edges of the cosine-bell apodization used for the intensity observations.

and $\mathrm{d}\Omega = \sin\theta \mathrm{d}\theta \mathrm{d}\phi$. The integral extends in θ and ϕ to cover the visible fraction of the Sun.

The sensitivity function $[J]$ is often assumed to be equivalent to the limb-darkening function $[I]$, although this is not necessarily the case. In principle, the sensitivity function can be empirically computed from the observations by computing the RMS of the oscillatory signal as a function of position on the solar disk and reducing it to a function of μ, the fractional radius. Hence, I computed the RMS of the residual intensity signal after detrending the images, using HMI continuum images taken on ten consecutive days, for six different years. I detrended the images using a 15-minute running mean, and using the time series of residuals images, I then computed the mean and RMS around the mean of the residual signal, rebinned as a function of fractional radius $[\mu]$ and normalized to unity at disk center. The solar limb darkening for a set of wavelengths has been measured and is reported by Pierce and Slaughter (1977).

The empirical sensitivity functions that I derived for each year, the average for the six years, and the limb-darkening profiles given in Pierce and Slaughter (1977) interpolated at $\lambda = 617.3$ nm, the wavelength at which HMI is observing (Schou *et al.*, 2012; Couvidat *et al.*, 2012, 2016), and the profiles used by the Stanford group (T.P. Larson, 2017, private communication) are all compared in Figure 1. One additional complication is the behavior

near the limb of the different formulations of the polynomial representation of the limb darkening, given either as a function of $x = \ln(\mu)$ or μ; see Tables II or IV of Pierce and Slaughter (1977).

Since the intensity oscillatory signal is not attenuated by the line-of-sight projection, the apodization for the intensity images could be pushed closer to the edge of the solar disk without substantially adding noise, as in the case of velocity. The apodization was chosen by the Stanford group to start at $\mu = 0.98$, consisting of a cosine-bell attenuation that spans a range in μ of 0.015, as indicated by the vertical lines drawn in Figure 1.

The different profiles shown in Figure 1 are somewhat similar. Note how the empirical sensitivity profiles resulting from processing each of the six years are nearly identical. They deviate from the limb-darkening profiles, suggesting an increased sensitivity for $0.3 \leq \mu \leq 0.6$, and a sharper decrease in sensitivity for $\mu \geq 0.8$. In contrast, the different limb-darkening profiles are almost identical for $\mu < 0.9$, except that the polynomial parametrization in $x = \ln(\mu)$ leads to negative values close to the limb, including the one based on the Stanford version with two coefficients. The polynomial parametrization in μ of the limb darkening does not include the progressive attenuation near the limb resulting from an empirical determination of the sensitivity profile, although the contribution to the leakage matrix of the regions with $\mu \geq 0.98$ is dominated by the apodization.

The precise profile to be used for the computation of the intensity leakage matrix is yet to be determined. I opted to use a polynomial parametrization in μ, and either the limb darkening $[I(\mu)]$ given by the coefficients in Table IV of Pierce and Slaughter (1977), interpolated at $\lambda = 617.3$ nm, or a polynomial in μ fitted to my determination of the averaged empirical sensitivity function $[\bar{J}(\mu)]$ for all six years that were processed. I also used the leakage matrix computed by the HMI group at Stanford (T.P. Larsen, 2017, private communication).

1.3.2. Computation and Validation of the Leakage Matrix

A leakage matrix is simply computed by generating images representing the quantity $J(\mu)Y_\ell^{m*}(\theta,\phi)$, or $I(\mu)Y_\ell^m(\theta,\phi)$ and processing them using the same spatial decomposition as for the observations.

The effects of the actual orientation, *i.e.* $P_{\rm eff}$, the effective position angle and B_o, the latitude at disk center $[D^o_\odot]$ the finite observer-to-Sun distance, and the image pixelization, while not described explicitly here, are taken into account when computing the images that are decomposed to generate a leakage matrix (see Schou, 1999; Korzennik, Rabello-Soares, and Schou, 2004). My computation evaluated $C_{\ell,m}(\delta\ell,\delta m) = C(\ell,m;\ell',m')$ for $\delta\ell = \pm 20$ and $\delta m = \pm 20$, while the HMI group at Stanford limited their evaluation to $\delta\ell = \pm 6$ and $\delta m = \pm 15$, where $\delta\ell = \ell' - \ell$ and $\delta m = m' - m$.

In an attempt to validate the different computations of leakage matrices suitable for intensity observations, I chose to compare the variation with respect to m (or the ratio m/ℓ) of the leakage to the variation of the observed power.

We can assume that the mode amplitude ought to be uniform with m, in the absence of any physical mechanism that would modulate the amplitude with m. If this is indeed the case, the variation of the observed total power, or the measured power amplitude of the modes, is only the result of the variation of the leakage matrix with m. Therefore the total power variation with m at a fixed ℓ should be proportional to the sum of sensitivity of the target mode plus the contribution of the leaks. We can thus equate the normalized total power

$$\bar{P}^{\rm Tot}_{\ell,m} = \frac{1}{P_{\rm N}} = \Sigma_\nu P_{\ell,m}(\nu) \tag{5}$$

to

$$\bar{Q}^{\mathrm{Tot}}_{\ell,m} = \frac{1}{Q_{\mathrm{N}}} \Sigma_{\delta\ell,\delta m} C^2_{\ell,m}(\delta\ell, \delta m), \tag{6}$$

where P_{N} and Q_{N} are normalization factors chosen to set $\bar{Q}^{\mathrm{Tot}}_{\ell,m=0} = \bar{P}^{\mathrm{Tot}}_{\ell,m=0} = 1$.

On the other hand, the modes' observed power amplitude $[A_{n,\ell,m}]$ as measured by fitting the modes should be proportional to the values of the $\delta\ell = \delta m = 0$ leak, or $C^2_{\ell,m}(0,0)$. Hence the quantity

$$\bar{A}_{\ell,m} = \frac{1}{A_{\mathrm{N}}} \Sigma_n A_{n,\ell,m} \tag{7}$$

is equal to the ratio

$$\bar{Q}_{\ell,m} = \frac{C^2_{\ell,m}(0,0)}{C^2_{\ell,m=0}(0,0)} \tag{8}$$

if A_{N} is such that $\bar{A}_{\ell,m=0} = 1$, since $\bar{Q}_{\ell,m=0} = 1$ by construction.

In order to increase the statistical significance for the observed quantities $\bar{P}^{\mathrm{Tot}}_{\ell,m}$ and $\bar{A}_{\ell,m}$, I performed additional averaging over a range in ℓ ($\delta\ell = \pm 1$), plus some smoothing over m and symmetrization in m.

Figures 2, 3, and 4 show these comparisons, using three distinct leakage matrices and a set of degrees. While the overall variation with m/ℓ agrees qualitatively, none of the leakage matrices leads to $\bar{Q}^{\mathrm{Tot}}_{\ell,m}$ or $\bar{Q}_{\ell,m}$ profiles that closely match the observed quantities, $\bar{P}^{\mathrm{Tot}}_{\ell,m}$ or $\bar{A}_{\ell,m}$ respectively. Moreover, the two methods do not agree as to which case best models the observed quantities. This apparent contradiction could be the result of the wrong assumption that the mode power is independent of m. Since it is the solar rotation that breaks the spherical symmetry and thus "defines" m, it is not inconceivable that while the solar rotation is slower than the oscillations, the rotation attenuates some azimuthal orders over others and produces an intrinsic variation of the mode amplitude with azimuthal order, m. Alternatively, it has been shown that the latitudinal magnetic field distribution modulates the mode power distribution with m (Komm, Howe, and Hill, 2002), and thus that distribution might contribute to explaining this discrepancy.

1.4. Seed Asymmetry for Intensity

Using high-degree resolved modes, Duvall *et al.* (1993) were the first to note that not only are the profiles of the modes asymmetric, but the asymmetry for velocity observations is of the opposite sign to the asymmetry for intensity observations. This asymmetry is, of course, also present at low and intermediate degrees, and it is observed, as expected, to be of opposite sign for velocity and intensity.

For each mode set, the fitting starts from some initial guess, also known as a seed. The seed file holds the list of modes to attempt to fit, *i.e.* the coverage in (n, ℓ), and for each mode a rather good initial guess of the mode's central frequency, or multiplet, the frequency splitting parametrized by a polynomial expansion in m, its line width, and its asymmetry. The initial guesses for the asymmetry are set to be a smooth function of frequency, and for velocity observations, using my parametrization, these are mostly negative. Since the asymmetry of the intensity observations is of the opposite sign, a new seed asymmetry had to be computed.

To accomplish this, I ran my second step, or initial fit, as described earlier in Section 1.2, using one 72-day long segment, and using at first the negative initial guesses for α ap-

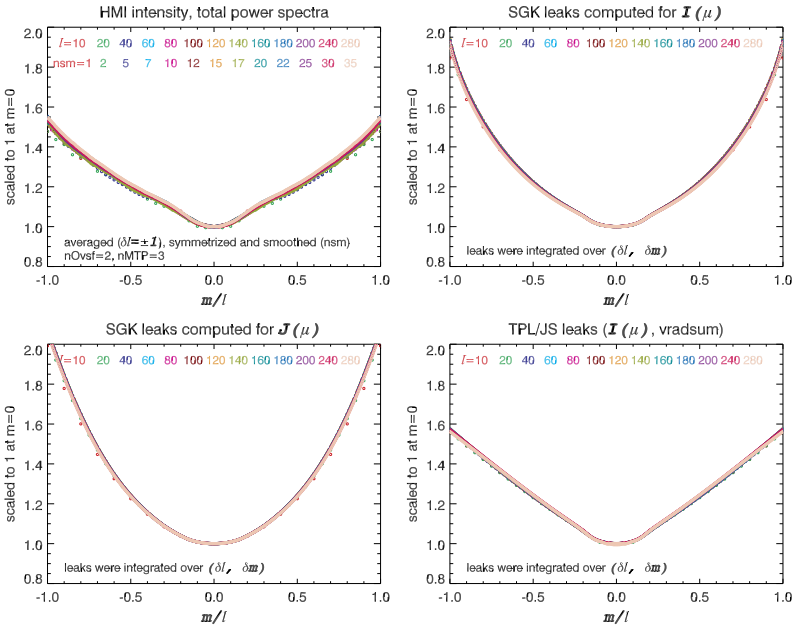

Figure 2 *Upper-left panel*: total power in the power spectra of the HMI intensity oscillation signal for a set of degrees, $\ell = 10, 20, (20), 200, (40), 280$, plotted as a function of the ratio m/ℓ, and normalized to unity at $m = 0$. The total power was smoothed in m (as indicated by the *nsm* key) and symmetrized with respect to m/ℓ, and estimated using a $\delta\ell = \pm 1$ range in ℓ to increase the significance of the derived profiles. The *other three panels* show the sum of the leaks for the same set of degrees, also plotted as a function of the ratio m/ℓ, and normalized to unity at $m = 0$, *i.e.* $\bar{Q}^{\rm Tot}_{\ell,m} = \frac{1}{Q_{\rm N}} \Sigma_{\delta\ell,\delta m} C^2_{\ell,m}(\delta\ell, \delta m)$. Each of these three panels corresponds to leakage estimates based on different $J(\mu)$ or $I(\mu)$ profiles.

propriate for velocity observations, *i.e.* $\alpha^{sV}_{n,\ell}$. The resulting fitted asymmetries were mostly positive. I proceeded to fit a polynomial in ν to them and produced updated guesses for intensity observations, *i.e.* $\alpha^{sI}_{n,\ell}$. I repeated this procedure six times, as illustrated in Figure 5, until the resulting mean change in the resulting fitted frequencies was negligible. The final parametrization of the initial guess for $\alpha^{sI}_{n,\ell}$ was subsequently used to fit all of the intensity observations.

2. Fitting Results

For reasons of convenience explained earlier, the time series of spherical harmonic coefficients computed by spatially decomposing HMI continuum intensity images have not been gap-filled. I computed sine multi-tapered power spectra for four consecutive 72-day long time series and one 288-day long time series. The power spectra were fitted using my fitting method, using the seed file adjusted to take into account the mode profile asymmetry for intensity observations, and two sets of leakage matrices: one computed by myself based on the limb darkening, parametrized by a five-coefficient polynomial in μ (Pierce and Slaughter, 1977, interpolated at $\lambda = 617.3$ nm) and one provided by the HMI group at Stanford (T.P. Larson and J. Schou, 2017, private communication).

Only the 72-day long time series were fitted using both leakage matrices and using an asymmetric profile. All of the other cases were fitted using only the leakage matrix that

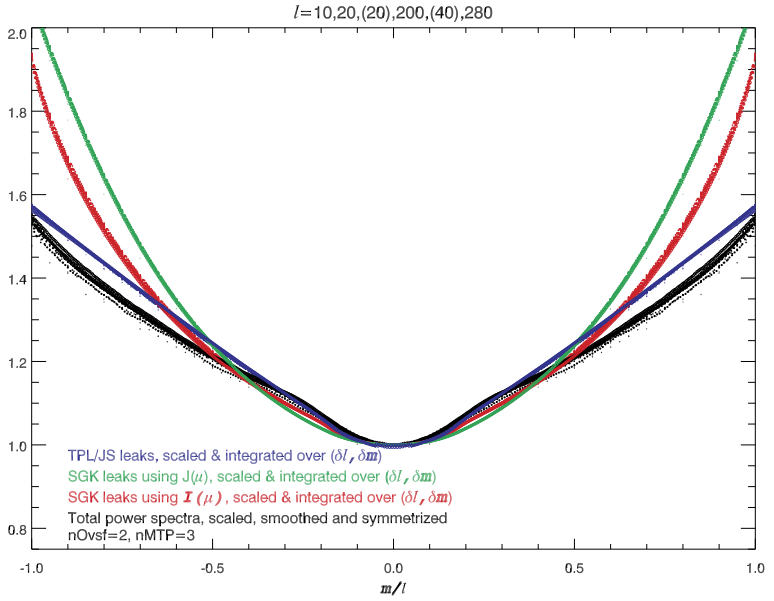

Figure 3 Direct comparison of the profiles shown in Figure 2, with the size of the symbols proportional to ℓ. Note how none of the leakage computations matches the observed total power, nor do they correctly duplicate the distinctive kink near $m/\ell = 0.25$ seen in the power profiles, although the case computed by me, using $I(\mu)$, displays a hint of a qualitatively similar kink.

I computed, based on a limb-darkening profile. In order to assess the effect of fitting the asymmetry, I also fitted the intensity data with a symmetric profile. This was accomplished by modifying the seed file to set the asymmetry to zero, and changing the steps used in the fitting procedure to leave the asymmetry parameter null by never including it in the list of parameters to fit.

2.1. Intensity S/N Limitation

A major difference between velocity and intensity oscillatory signals, in addition to the sign of the asymmetry, is the nature of the so-called background noise, which is so called because it is a signal of solar origin that adds a noisy background level to the oscillatory signal. Intensity observations, whether disk integrated or resolved, show a noise contribution that increases as the frequency decreases, of a ν^{-1} nature. The detrending that was adequate for the velocity signal is no longer optimal for intensity; hence I modified the detrending that I performed on the time series before computing the sine multi-taper power spectrum, from subtracting a 20-minute running mean to subtracting an 11-minute running mean. This filters out power below 1.52 μHz rather than below 0.83 μHz.

Since my fitting method performs a so-called "sanity check" at regular intervals, modes at low frequencies, where the background level is high for intensity observations, are no longer fitted. This attrition at low frequencies is illustrated in Figure 6, where the (n, ℓ, m) singlets that were successfully fitted are shown in an ℓ–ν diagram and compared to the same representation when fitting a similar dataset derived from gap-filled velocity observations.

Because the coverage in the ℓ–ν space is much more sparse for intensity, I revised the procedure that I used to derive multiplet characteristics from fitted singlets, *i.e.* characteristics derived for all the peaks of a given (n, ℓ) from all the (n, ℓ, m) singlets. This procedure

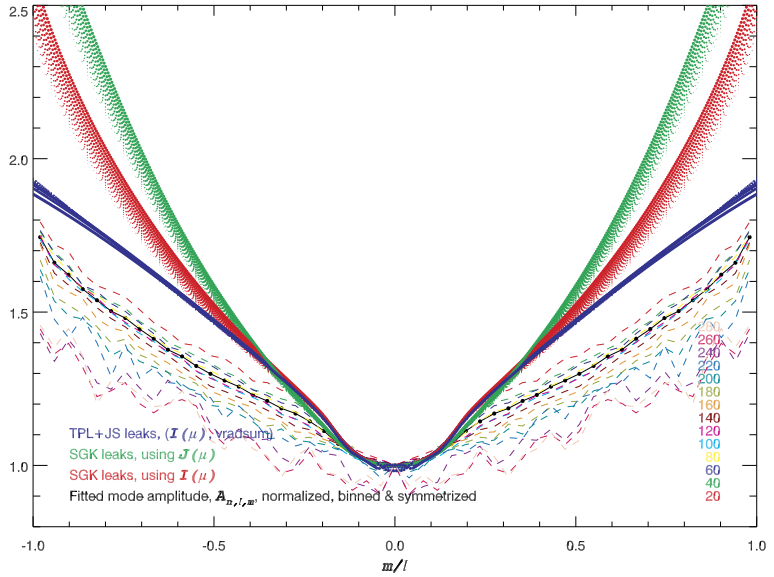

Figure 4 Comparison, like the one shown in Figure 3, but using the fitted mode power amplitude $[A_{n,\ell,m}]$ to estimate the normalized and symmetrized observed power distribution profile with respect to m/ℓ and shown as the *connected filled circles*. The normalized values $\bar{Q}_{\ell,m} = \dfrac{C^2_{\ell,m}(0,0)}{C^2_{\ell,0}(0,0)}$, *i.e.* no summation on $(\delta\ell, \delta m)$, are shown with *colored filled circles*, with their size being proportional to ℓ. The *colored-dashed lines* correspond to estimates of the observed power distribution profile, derived from measured $A_{n,\ell,m}$ but restricted to a given range in ℓ centered around a target ℓ. Note how again none of the leakage computations matches the mode-profile power amplitude, nor do they correctly duplicate the distinctive kink seen in the observations, although the case computed by me and by the Stanford group, both using $I(\mu)$, displays a hint of a qualitatively similar kink.

fits a Clebsch–Gordan polynomial to all of the successfully fitted frequencies, $\nu_{n,\ell,m}$, for a given (n, ℓ) as a function m to derive a mode frequency $[\nu_{n,\ell}]$ and frequency-splitting coefficients. The procedure fits from one to nine coefficients, performs a 3σ rejection of outliers, and computes a mode multiplet if, and only if, at least one in eight of all the expected m are used in the polynomial. This criterion worked well when fitting velocity observations, but it eliminates most of the low-order, low-frequency modes, including all of the f-modes when fitting intensity observations.

I readjusted this procedure to derive a second set of multiplets using a less stringent constraint, namely that at least *only* one in 16 of all the m could be fitted. This led to some outliers that were then cleaned out by eliminating modes whose frequency does not fall on a smooth function of ℓ for each order, n. This is illustrated in Figure 6 by the green dots.

2.2. Effect of Gap-Filling and Longer Time Series on Low-Frequency Noise

Since the time series of intensity spherical harmonic coefficients were not gap-filled, I checked the contribution of the gaps to the background noise. A naive estimate, illustrated in Figure 7, suggests that gaps scatter a great deal of power into a higher background noise, including at low frequencies. I therefore adapted the gap filler that I use for the GONG observations to gap-fill one 72-day long time series of HMI intensity data. This gap filler is the same as the one used by the Stanford group to gap-fill the MDI and HMI velocity data.

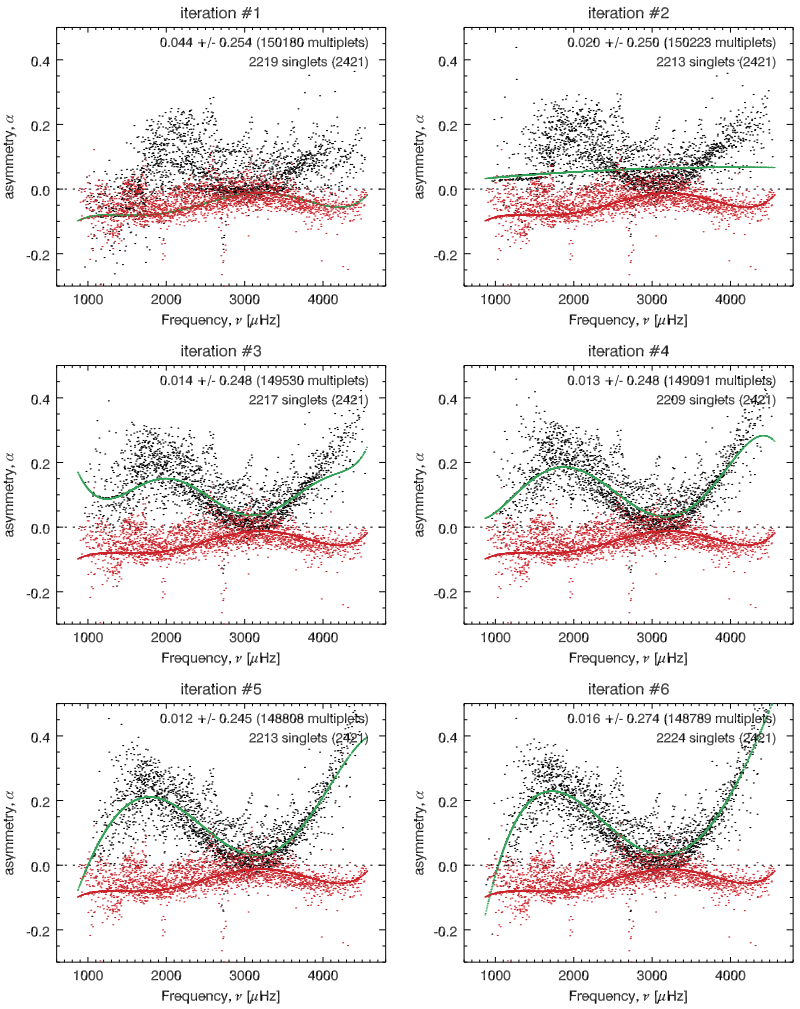

Figure 5 Values of the seed, *i.e.* initial guess, and fitted asymmetry, plotted as a function of frequency, for each iteration used in the refinement of the seed asymmetry values. The *red dots* are values of $\alpha^V_{n,\ell}$ resulting from fitting velocity observations, and the *black dots* are values of $\alpha^I_{n,\ell}$ resulting from fitting intensity observations at each successive iteration. The *red curves* show the seed asymmetry $[\alpha^{sV}_{n,\ell}]$ used for the velocity, the *green curves* show the seed asymmetry $[\alpha^{sI}_{n,\ell}]$ for the intensity at each iteration. The mean and standard deviation of the changes in the fitted frequency values at each iteration are indicated in each panel. Note how even with initial negative values for the asymmetry, the resulting fitted asymmetries become mostly positive at the first iteration (*upper-left panel*).

Figures 8 to 13 show that neither gap-filling nor using longer time series reduces the low-frequency background noise. Figures 8 and 9 show that i) gap-filling the intensity observations barely changes the background levels, ii) the background level for the intensity is about 20 times higher around 2 mHz than for the velocity, and iii) the longer time series do not lower the background, but reduce the background realization noise. For the intensity observations, this reduction is not sufficient to see the low-order, low-frequency modes. Note

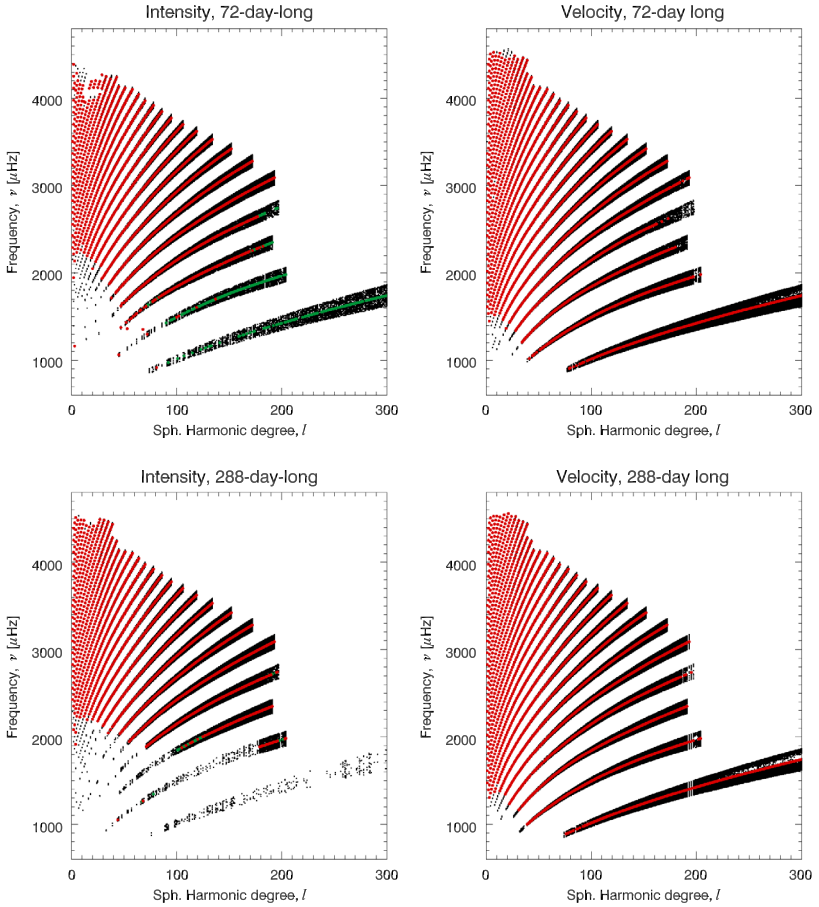

Figure 6 Coverage in the ℓ–ν plane of the fitted modes. *Black dots* show singlets, *red dots* multiplets, and *green dots* multiplets resulting from a less restrictive rule for the conversion of singlets into multiplets (see explanation in the text). The *top two panels* correspond to fitting one 72-day long time series, the *bottom two panels* to fitting one 288-day long time series. *Panels on the left* correspond to intensity observations, *panels on the right* to coeval velocity observations. Note the reduced success rate in fitting intensity observations, especially for the low-order, low-frequency modes. Note also the counter-intuitive higher success rate for fitting f-mode singlets for the 72-day long time series than for the 288-day long series when using intensity observations.

also the clearly visible change of sign of the mode-profile asymmetry between intensity and velocity power spectra.

Figures 10, 11, 12, and 13 show i) how the realization noise produces spikes that without a proper sanity check can be easily confused with low-amplitude modes, and ii) that some modes peak above the noise in an m-averaged spectrum, but cannot be distinguished from the noise when fitting singlets.

From these figures, one concludes that the power at low frequency is of solar origin and masks the oscillatory signal. The power scatter by the gaps at these frequencies is negligible, while increasing the length of the time series decreases the realization noise, but not the background level. Eventually, a very long time series may bring the realization noise to a level low enough to see a weak oscillatory signal emerge clearly above the background, but

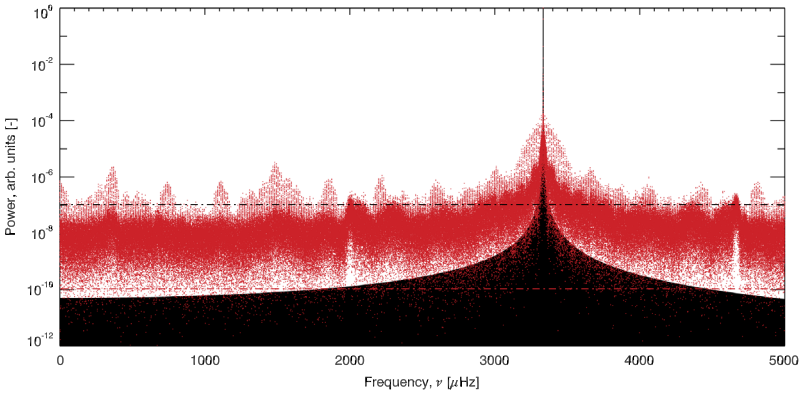

Figure 7 Effect of gaps on a noiseless data set. The *black curve* is the power spectrum of a simple sine wave, sampled every 45 seconds for 288 days. The *red curve* is the same sine wave, but with values set to zero at times when HMI observations are missing for the 288-day long time series. The introduction of gaps scatters power and raises the background levels considerably but uniformly with respect to the frequency compared to the gap-less noiseless case.

quadrupling the length is not enough. In fact, and somewhat counter-intuitively, quadrupling the length of the time series resulted in making fitting low frequency modes more difficult.[4]

For completeness, I also fitted the 288-day long time series using gap-filled time series. As anticipated, the resulting number of fitted modes and their characteristics are barely different from the raw data: a few more singlets were fitted, but the same number of multiplets were derived when the observations were gap-filled. The mean of the difference between raw and gap-filled data in the derived frequencies is smaller than 1 nHz, with a standard deviation of 13 nHz, and differences in the derived FWHM and asymmetry are negligible.

2.3. Results from 72-Day and 288-Day Fitting

Figures 14 and 15 show mode characteristics resulting from fitting 72-day and 288-day long time series after converting singlets to multiplets. Table 2 lists the number of fitted modes (singlets) and the number of derived multiplets for each fitted time series, the different type of data, and the leakage matrix. The FWHM $[\Gamma_{n,\ell}]$, the asymmetry $[\alpha_{n,\ell}]$, the uncertainty of the fitted frequencies $[\sigma_{\nu_{n,\ell}}]$, and the mode power amplitudes $[\bar{A}_{n,\ell}]$ are plotted for the resulting multiplets for one representative 72-day long set and for the 288-day long set. The corresponding values derived from fitting coeval velocity observations are shown as well.

Except for the low-order, low-frequency modes, the FWHM and the frequency uncertainties derived using either velocity or intensity observations agree quite well. As expected, the asymmetry derived from intensity observations is of opposite sign to the asymmetry derived from velocity observations, but it is also larger in magnitude by about a factor two. The mode-power amplitude variation with frequency is overall similar, whether measured using intensity or velocity observations, as it peaks at the same frequency, but it shows a somewhat different distribution. This is most marked for results from fitting 72-day long time series and at low frequencies. Most of the additional low-frequency modes derived from the 72-day long time series, using a less stringent constraint to derive multiplets, show consistent values that mostly agree with their velocity counterparts, except for higher uncertainties and

[4]The cause of this remains to be further investigated.

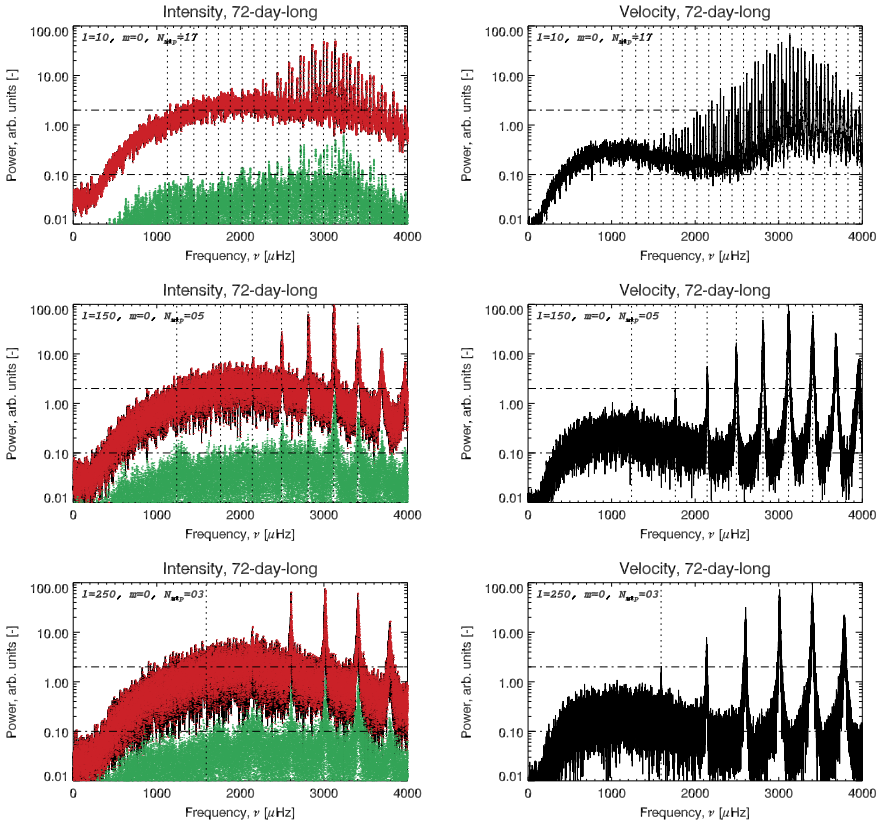

Figure 8 Examples of sine multi-taper zonal ($m = 0$) power spectra computed using 72-day long time series. The *panels in the first column* show power spectra of intensity observations derived from raw or gap-filled time series (*red and black curves,* respectively). The *green curves* are the difference between the spectra computed using raw or gap-filled time series. The *panels in the second column* show power spectra of gap-filled coeval velocity observations. The *vertical lines* indicate the location of the modes being fitted. Each *row* corresponds to a different value of ℓ ($\ell = 10, 150, 250$, top to bottom, respectively), the *horizontal lines* are drawn as fiducial lines to mark the background level around 2 mHz.

a larger FWHM at the lowest frequencies. The higher uncertainty in itself is not surprising since these multiplets are derived from fewer singlets, but the increase in FWHM cannot be easily explained.

When we compare the results from fitting a 72-day long time series to those resulting from fitting the 288-day long series, we observe the following: the mode FWHM, frequency uncertainty, asymmetry, and power amplitude distribution are comparable, although i) very few low-frequency modes are successfully derived; ii) the frequency uncertainty is reduced as expected by about a factor two, namely the square root of the ratio of the time-series lengths; and iii) the scatter in the measured asymmetry is reduced for the intensity as it is for the velocity.

I have yet to fully understand why, when using the longer time series, almost no modes below $\nu < 1800$ μHz or $\Gamma < 0.8$ μHz could be fitted (see Figure 6). This may suggest that despite appearing consistent, the low-frequency modes derived using a shorter time

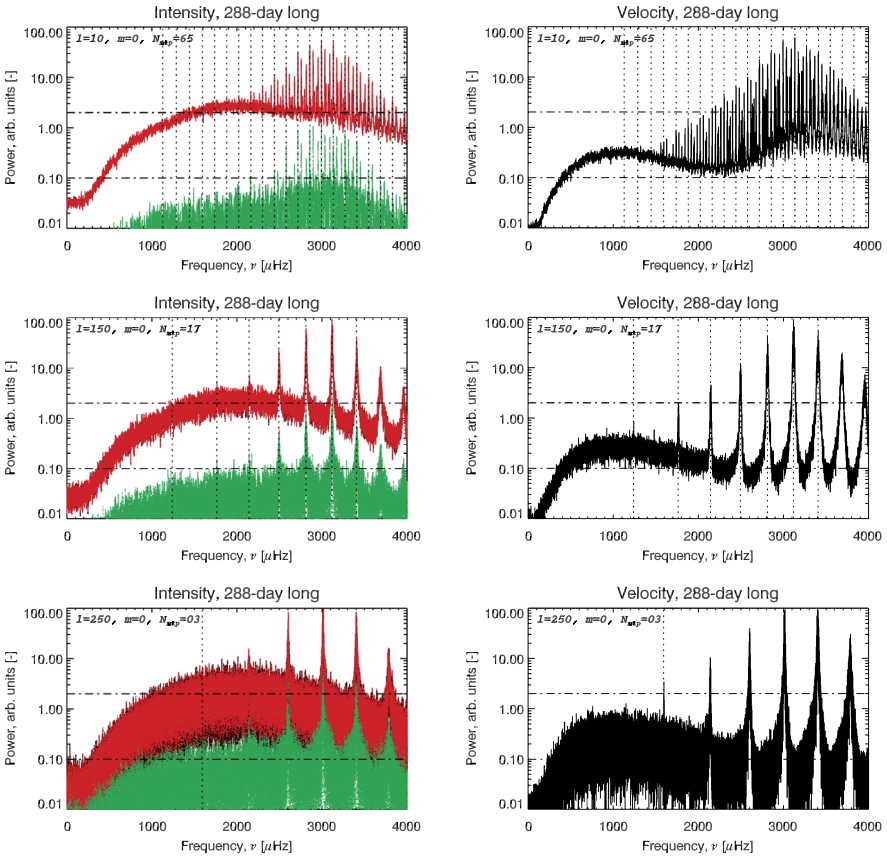

Figure 9 Examples of sine multi-taper zonal ($m = 0$) power spectra computed using 288-day long time series. The *panels in the first column* show power spectra of intensity observations derived from raw or gap-filled time series (*red and black curves*, respectively). The *green curves* are the difference between the spectra computed using raw or gap-filled time series. The *panels in the second column* show power spectra of gap-filled coeval velocity observations. The *vertical lines* indicate the location of the modes being fitted. Each *row* corresponds to a different value of ℓ ($\ell = 10, 150, 250$, top to bottom, respectively), the *horizontal lines* are drawn as fiducial lines to mark the background level around 2 mHz.

series are suspicious and the method, especially the sanity check, needs to be adapted to the specifics of the noise distribution of the intensity signal.

2.4. Comparison Using Different Leakage Matrices

Figures 16 and 17 show a comparison of the mode parameters inferred by fitting the same time series of intensity observations, using the exact same method, but two different estimates of the leakage matrix. Despite the different signature of the leakage sensitivity with m, the resulting fitted frequencies, and most of the other modes parameters, are barely different and show no systematic trends. Comparisons of the singlets' frequency, or the singlets' scaled[5] frequency, show a normal distribution with no significant bias and very low scat-

[5]The scaling is made by dividing the difference by its uncertainty.

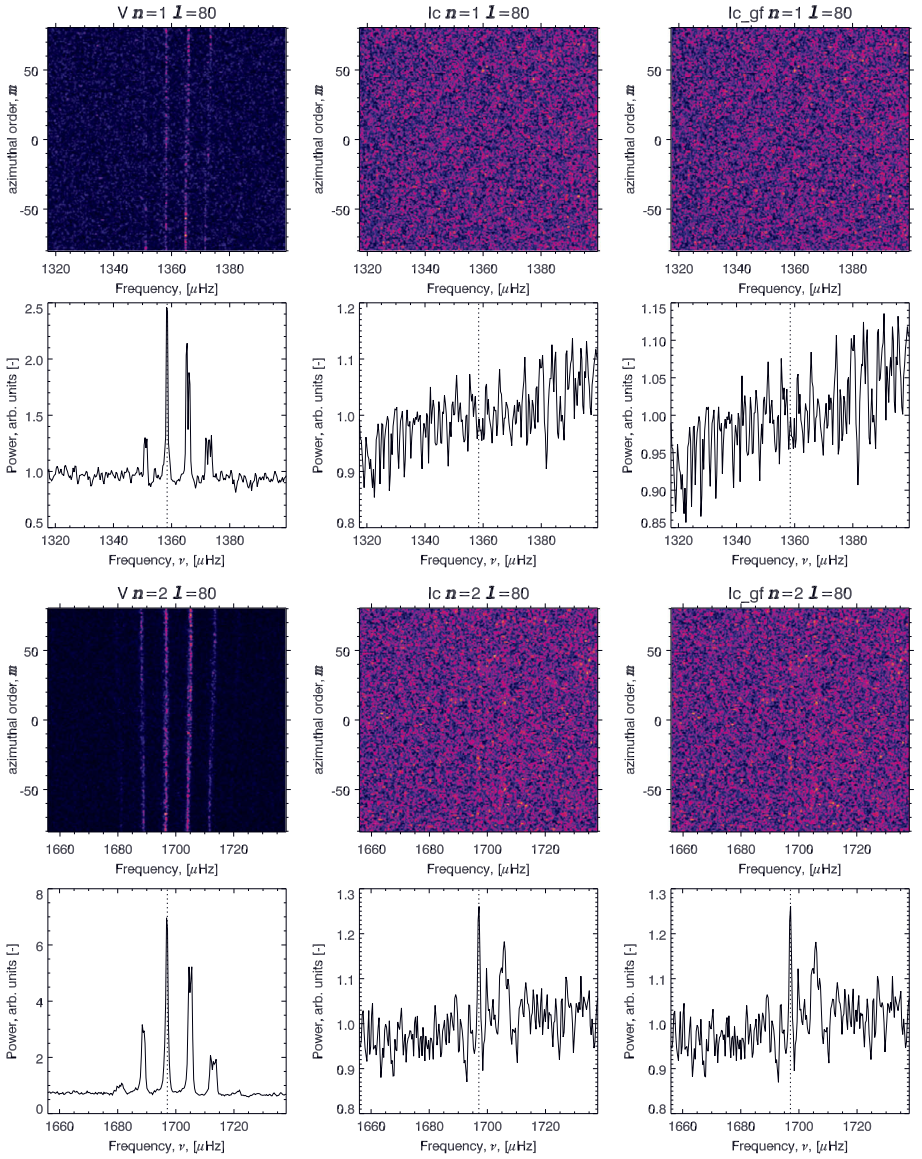

Figure 10 Stacked sections of power spectra, shown as a function of ν and m, and the corresponding m-averaged spectra, centered around a set of two modes for $(n, \ell) = (1, 80)$ and $(2, 80)$, computed using a 72-day long time series. *Each set of six panels* shows in the *top row* the stacked spectra, in the *bottom row* the corresponding m-averaged spectrum, and from *left to right*, spectra computed from the gap-filled velocity, the raw (*i.e.* with gaps) intensity, and the gap-filled intensity coeval time series. The *vertical lines* indicate the mode frequency. Stacked sections of power spectra are sections of spectra centered on the mode singlet frequency $[\nu_{n,\ell,m}]$ computed using a very good estimate of the mode frequency and frequency splitting to offset in frequency the spectrum for each m so as to coalign the target modes.

ter. Only the mode line-width $[\Gamma]$ is systematically different when we fit the longer time series, although not significantly so. Of course, we cannot rule out that fitting much longer

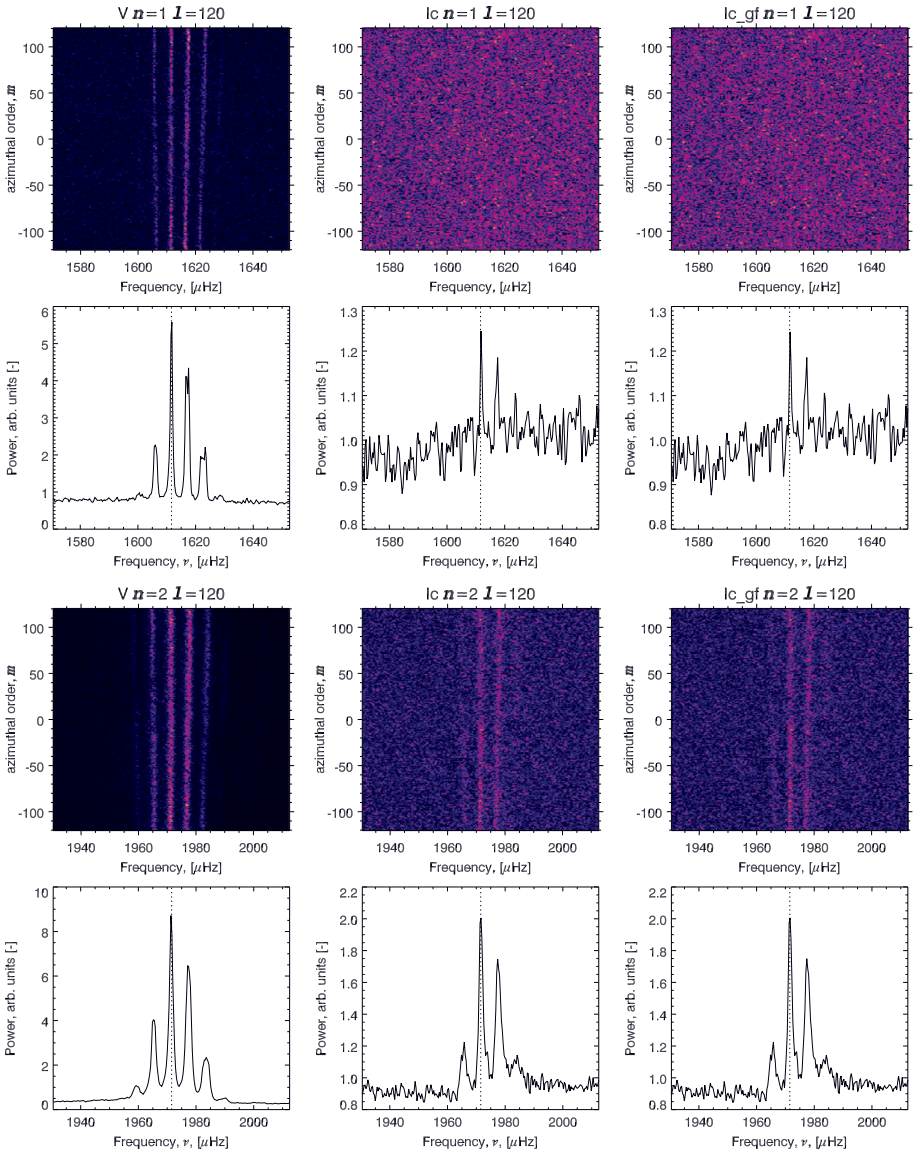

Figure 11 Stacked sections of power spectra, shown as a function of ν and m, and the corresponding m-averaged spectra, centered around a set of two modes for $(n, \ell) = (1, 120)$ and $(2, 120)$, computed using a 72-day long time series. *Each set of six panels* shows in the *top row* the stacked spectra, in the *bottom row* the corresponding m-averaged spectrum, and from *left to right*, spectra computed from the gap-filled velocity, the raw (*i.e.* with gaps) intensity and the gap-filled intensity coeval time series. The *vertical lines* indicate the mode frequency. Stacked sections of power spectra are sections of spectra centered on the mode singlet frequency $[\nu_{n,\ell,m}]$ computed using a very good estimate of the mode frequency and frequency splitting to offset in frequency the spectrum for each m so as to coalign the target modes.

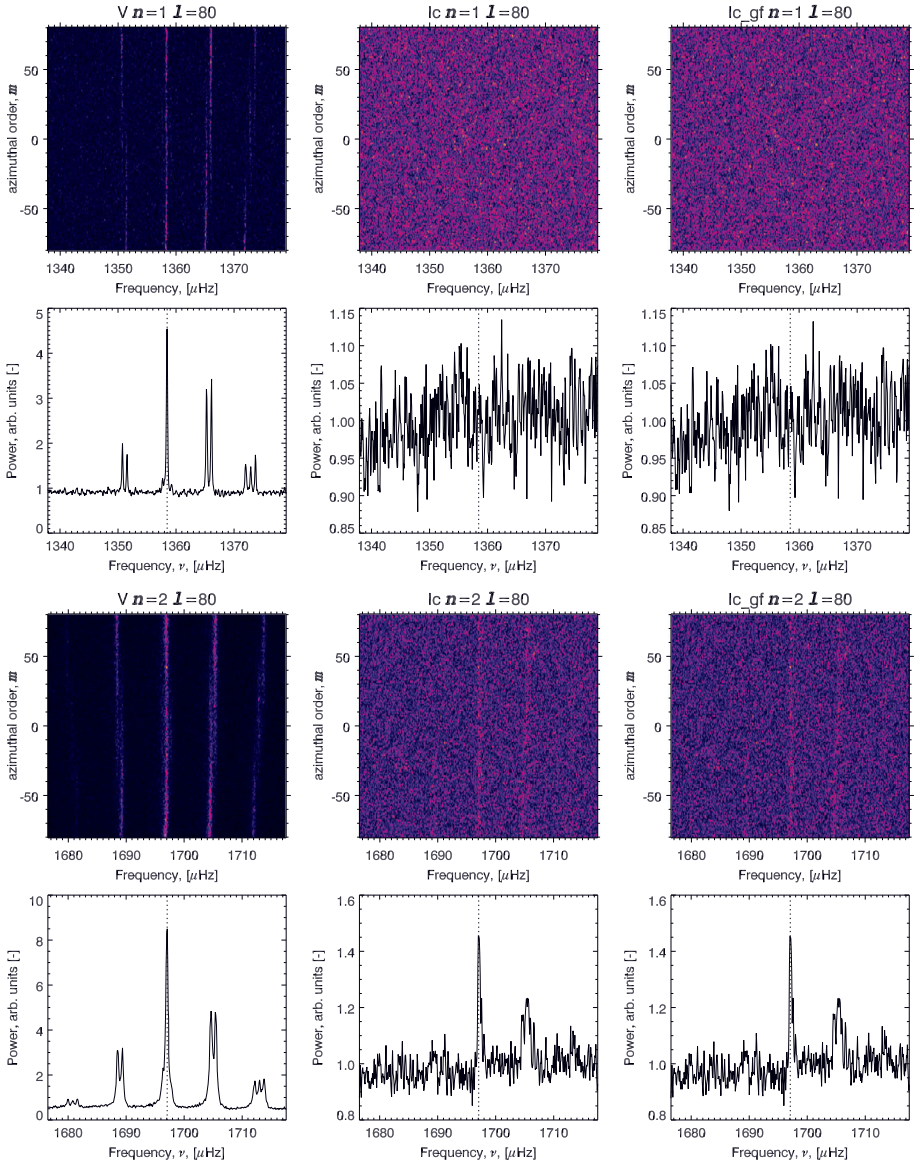

Figure 12 Stacked sections of power spectra, shown as a function of ν and m, and the corresponding m-averaged spectra, centered around a set of two modes for $(n, \ell) = (1, 80)$ and $(2, 80)$, as in Figure 10, but computed using a 288-day long time series. *Each set of six panels* shows in the *top row* the stacked spectra, in the *bottom row* the corresponding m-averaged spectrum, and from *left to right*, spectra computed from the gap-filled velocity, the raw (*i.e.* with gaps) intensity and the gap-filled intensity coeval time series. The *vertical lines* indicate the mode frequency. Stacked sections of power spectra are sections of spectra centered on the mode singlet frequency $[\nu_{n,\ell,m}]$ computed using a very good estimate of the mode frequency and frequency splitting to offset in frequency the spectrum for each m so as to coalign the target modes. The $(n, \ell) = (2, 80)$ modes become barely visible in intensity when using a longer time series.

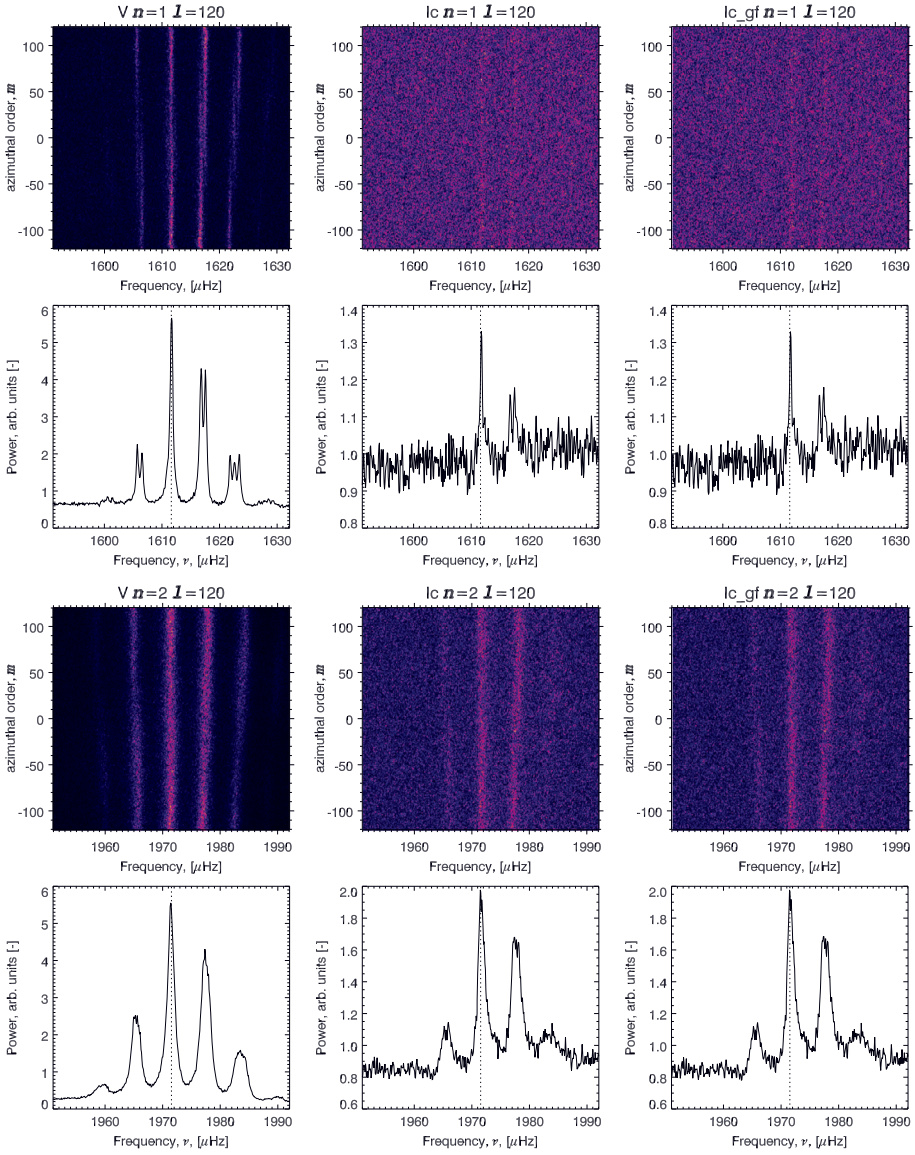

Figure 13 Stacked sections of power spectra, shown as a function of ν and m, and the corresponding m-averaged spectra, centered around a set of two modes for $(n, \ell) = (1, 120)$ and $(2, 120)$, as in Figure 11, but computed using a 288-day long time series. *Each set of six panels* shows in the *top row* the stacked spectra, in the *bottom row* the corresponding m-averaged spectrum, and from *left to right*, spectra computed from the gap-filled velocity, the raw (*i.e.* with gaps) intensity and the gap-filled intensity coeval time series. The *vertical lines* indicate the mode frequency. Stacked sections of power spectra are sections of spectra centered on the mode singlet frequency $[\nu_{n,\ell,m}]$ computed using a very good estimate of the mode frequency and frequency splitting to offset in frequency the spectrum for each m so as to coalign the target modes. The $(n, \ell) = (1, 120)$ modes become barely visible in intensity when using a longer time series.

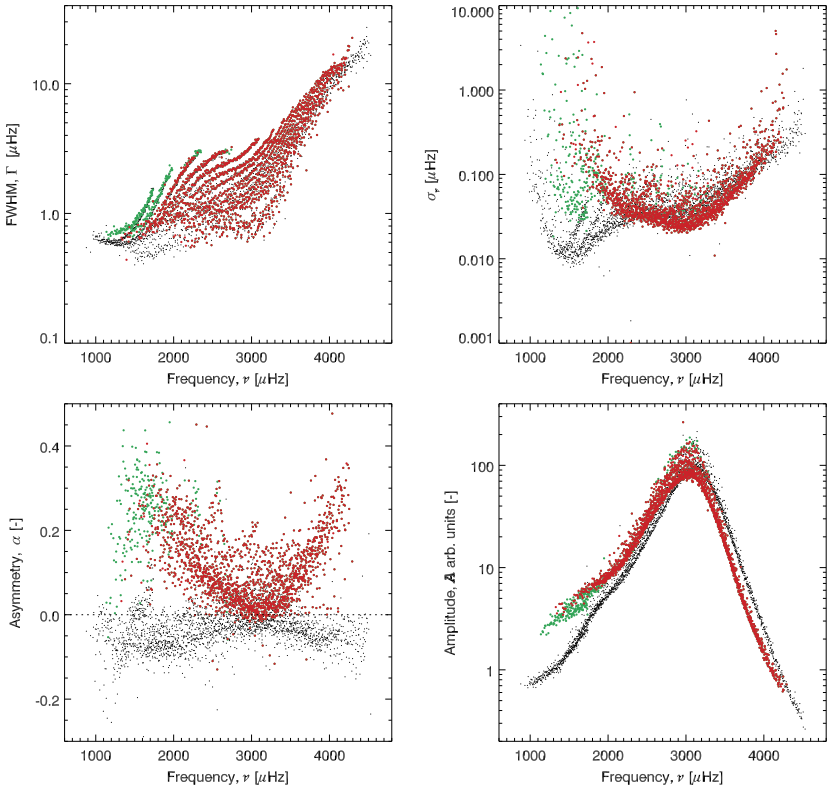

Figure 14 Mode characteristics derived from fitting a 72-day long time series after converting singlets to multiplets. The *panels* show as a function of frequency the mode FWHM [Γ], the frequency uncertainty [σ_ν], the asymmetry [α], and the mean mode amplitude [$\bar{A}_{n,\ell} = \frac{1}{Nm} \Sigma_m A_{n,\ell,m}$]. The *red and green circles* correspond to fitting intensity observations, with the *green circles* resulting from a less restrictive constraint in the conversion of singlets into multiplets (see text and Figure 6), the *black dots* correspond to results from fitting coeval velocity time series. Except for the low-order, low-frequency modes, the FWHM and the frequency uncertainties derived using either velocity or intensity agree quite well. The asymmetry when fitting intensity observations is of opposite sign to the asymmetry for velocity, but also larger in magnitude. The mode power amplitude distribution, while peaking at the same frequency and being similar overall, shows a distinctive different distribution with frequency when fitting intensity rather than velocity observations. The *green circles*, resulting from estimating the multiplets using relaxed rules, appear to be consistent with their corresponding values derived from velocity, but show a larger uncertainty. This in itself is not surprising since they are derived from fewer individually fitted singlets.

time series may lead to small but significant or systematic differences. Still, this comparison shows that for the 72-day and 288-day long time series, the use of different leakage-matrix estimates does not really affect the fitted values.

2.5. Comparison with Results from Fitting the Velocity

Now that we have, for the first time, mode parameters resulting from fitting the same interval based on either velocity or intensity HMI observations, let us compare the resulting mode characteristics in detail. Even though the velocity time series were gap-filled while the intensity time series were not, we have shown that we can rule out that this affected the results

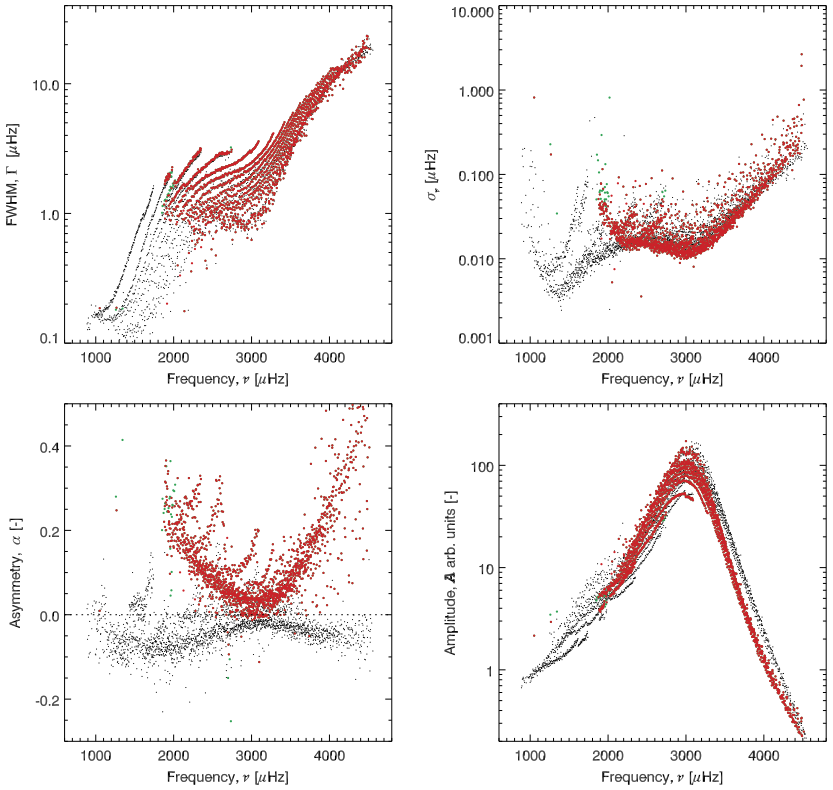

Figure 15 Mode characteristics derived from fitting a 288-day long time series after converting singlets to multiplets. The *panels* show as a function of frequency the mode FWHM [Γ], the frequency uncertainty [σ_ν], the asymmetry [α], and the mean mode amplitude [$\bar{A}_{n,\ell} = \frac{1}{N_m} \Sigma_m A_{n,\ell,m}$]. The *red and green circles* correspond to fitting intensity observations, with the *green circles* resulting from a less restrictive constraint in the conversion of singlets into multiplets (see text and Figure 6), the *black dots* corresponding to results from fitting coeval velocity time series. Again, like for the 72-day long results, the frequency uncertainties derived using either velocity or intensity observations agree quite well. The asymmetry for intensity observations is of opposite sign to the asymmetry for velocity observation and larger in magnitude. The mode power amplitude distributions derived from intensity or velocity observations also peak at the same frequency, but are also more similar than for the 72-day long case. The frequency uncertainties are, as expected, reduced by a factor $\sqrt{288/72} = 2$ when compared to values obtained using a shorter time series. By contrast to the 72-day long results, very few individual singlets were fitted for modes with $\nu < 1800$ μHz and $\Gamma < 0.8$ μHz.

and thus this comparison, because i) the fill factors are already high, and ii) the background signal at low frequency is anyway much higher for the intensity than for the velocity.

Figures 18 and 19 compare frequencies, scaled frequencies, scaled FWHM, and scaled asymmetries derived from coeval time series from either intensity or velocity observations for singlets or multiplets. The frequency comparisons show virtually no bias for the singlets, but some small bias for the multiplets (*i.e.* 0.43 and 0.86σ for the 72-day and 288-day long time series, respectively). Of course, the asymmetry differences are large and show a smooth trend with frequency.

Since I also fitted the data using a symmetric mode profile, I can repeat exactly the same comparison, but using mode characteristics derived from fitting a symmetric profile

Table 2 Number of fitted singlets and derived multiplets for different fitting cases.

Fitted profile	Asymmetric			
Time-series length	72 days			
Data type/Leakage	V/SU			
Start time	2010.04.30	2010.07.11	2010.09.21	2010.12.02
No. of singlets	205,530	206,251	204,956	204,969
No. of multiplets	2,297	2,296	2,287	2,294
Data type/Leakage	I/SU			
No. of singlets	149,420	148,457	146,072	147,952
No. of multiplets	1,679	1,669	1,649	1,675
Data type/Leakage	I/SGK			
No. of singlets	145,793	145,020	142,612	144,266
No. of multiplets	1,662	1,678	1,657	1,661
Time-series length	288 days			
Start time	2010.07.11			
Data type/Leakage	V/SU	I/SGK	I_{gf}/SGK	
No. of singlets	281,977	202,420	202,719	
No. of multiplets	2,386	1,682	1,682*	
Fitted profile	Symmetric			
Time-series length	72 days			
Data type/Leakage	V/SU			
Start time	2010.04.30	2010.07.11	2010.09.21	2010.12.02
No. of singlets	206,227	206,265	203,374	204,858
No. of multiplets	2,287	2,285	2,278	2,281
Data type	I/SGK			
No. of singlets	143,534	142,502	140,386	141,894
No. of multiplets	1,654	1,655	1,628	1,649
Time-series length	288 days			
Start time	2010.07.11			
Data type/Leakage	V/SU	I/SGK		
No. of singlets	282,787	196,639		
No. of multiplets	2,389	1,670		

*Although not the same set of (n, ℓ) values as I/SGK

for either type of observations or length of time series. This comparison is presented in Figures 20 and 21, and systematic differences with skewed distributions are clearly visible.

Table 3 summarizes the comparisons and lists the mean and standard deviation around the mean of the differences or scaled differences. Comparing results from fitting symmetric profiles clearly demonstrates that we need to include the asymmetry of the mode profile at low and intermediate degrees and not just at high degrees. While the differences are not very large in themselves, especially for the 72-day long times series singlets, they rise to the 2.3 and 5.9σ levels for multiplets derived from the 72-day and 288-day long time series, respectively. More to the point, however, these differences clearly show systematic trends.

Table 3 Mean and standard deviation around the mean of mode characteristic raw or scaled differences, computed using singlet or multiplet values, whether i) using different leakage-matrix evaluations, ii) using gap-filling or not, iii) using intensity or coeval velocity observations and fitting asymmetric profiles, and iv) again using intensity or coeval velocity observations, but fitting symmetric profiles.

Len. [d]	$\Delta\nu$ [μHz]	$\Delta\nu/\sigma_\nu$	$\Delta\Gamma/\sigma_\Gamma$	$\Delta\alpha/\sigma_\alpha$	No. of common modes	
Asymmetric fitting [I] different leakage matrices, *i.e.* SU minus SGK						
72	0.000 ± 0.015	0.001 ± 0.017			142,704	*singl.*
	0.001 ± 0.014	0.001 ± 0.016			141,645	
	0.000 ± 0.015	0.001 ± 0.016			139,598	
	0.000 ± 0.015	0.000 ± 0.017			141,164	
288	-0.000 ± 0.008	-0.000 ± 0.015			201,658	
72	0.000 ± 0.029	0.004 ± 0.233	-0.023 ± 0.060	-0.001 ± 0.071	1,653	*mult.*
	0.001 ± 0.021	0.025 ± 0.231	-0.021 ± 0.058	-0.002 ± 0.061	1,651	
	0.001 ± 0.023	0.014 ± 0.235	-0.017 ± 0.059	-0.004 ± 0.065	1,633	
	0.002 ± 0.032	0.017 ± 0.220	-0.019 ± 0.060	-0.001 ± 0.065	1,647	
288	0.000 ± 0.006	-0.000 ± 0.113	0.017 ± 0.055	0.001 ± 0.043	1,679	
Asymmetric fitting [I] gap-filled minus not gap-filling						
288	0.001 ± 0.013	0.001 ± 0.028			200,909	*singl.*
288	0.001 ± 0.006	0.023 ± 0.125	0.005 ± 0.035	0.005 ± 0.045	1,676	*mult.*
Asymmetric fitting, $I - V$						
72	0.015 ± 0.236	0.014 ± 0.289			115,347	*singl.*
	0.015 ± 0.239	0.011 ± 0.298			115,299	
	0.014 ± 0.238	0.011 ± 0.294			114,003	
	0.012 ± 0.236	0.008 ± 0.292			114,621	
288	0.021 ± 0.146	0.044 ± 0.296			191,979	
72	0.044 ± 0.113	0.470 ± 0.893	-0.065 ± 0.401		1,637	*mult.*
	0.049 ± 0.152	0.455 ± 0.854	-0.021 ± 0.354		1,658	
	0.035 ± 0.096	0.434 ± 0.864	-0.033 ± 0.370		1,637	
	0.033 ± 0.097	0.384 ± 0.844	-0.040 ± 0.369		1,640	
288	0.028 ± 0.053	0.856 ± 1.075	-0.008 ± 0.482		1,674	
Symmetric fitting, $I - V$						
72	0.118 ± 0.262	0.144 ± 0.312			114,581	*singl.*
	0.128 ± 0.265	0.153 ± 0.318			114,179	
	0.124 ± 0.263	0.149 ± 0.315			112,974	
	0.119 ± 0.261	0.146 ± 0.312			113,707	
288	0.161 ± 0.193	0.343 ± 0.350			188,372	
72	0.183 ± 0.225	2.133 ± 1.724	-0.040 ± 0.416		1,643	*mult.*
	0.173 ± 0.175	2.233 ± 1.729	-0.004 ± 0.346		1,642	
	0.165 ± 0.178	2.198 ± 1.780	-0.016 ± 0.375		1,621	
	0.183 ± 0.226	2.120 ± 1.726	-0.019 ± 0.379		1,636	
288	0.203 ± 0.256	5.395 ± 4.058	0.076 ± 0.483		1,662	

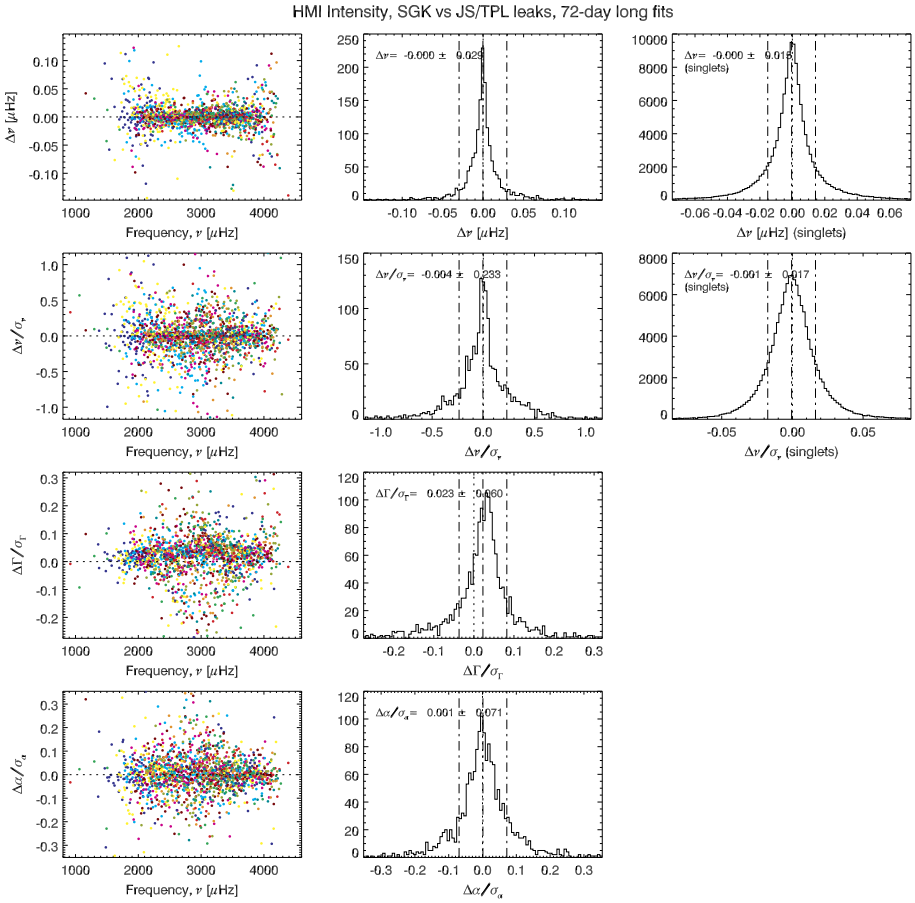

Figure 16 Comparison of mode characteristics derived from fitting a 72-day long time series after converting singlets to multiplets, and for singlets, using two different leakage-matrix computations, namely mine based on $I(\mu)$ and the one computed by the Stanford group. The *panels* show from top to bottom the raw and scaled frequency differences for multiplets and singlets, and the FWHM and asymmetry scaled differences. The *panels in the leftmost column* show the multiplet differences, with colors corresponding to the mode orders $[n]$. The *panels in the middle column* show the histogram distribution of the differences for the multiplets, while the *panels in the rightmost column* show the histogram distribution of the differences computed using singlets. *Vertical lines* are drawn at zero and at the mean plus or minus one standard deviation around the mean. Despite significant differences between the two leakage-matrix coefficients (see, for example, Figure 4), the resulting parameters show little differences in terms of both bias and spread. Only the FWHM differences show a non-negligible bias.

Close scrutiny of the table indicates a small residual bias in frequency differences from fitting co-eval velocity and intensity, even when using an asymmetric profile. It may well be that this small bias results from some remaining inadequacy in the fitting methods that is worth pursuing. This should not distract from the main conclusion that including the asymmetry is key in determining accurate mode characteristics that are consistent, regardless of whether they are measured using their manifestation from intensity or velocity fluctuations.

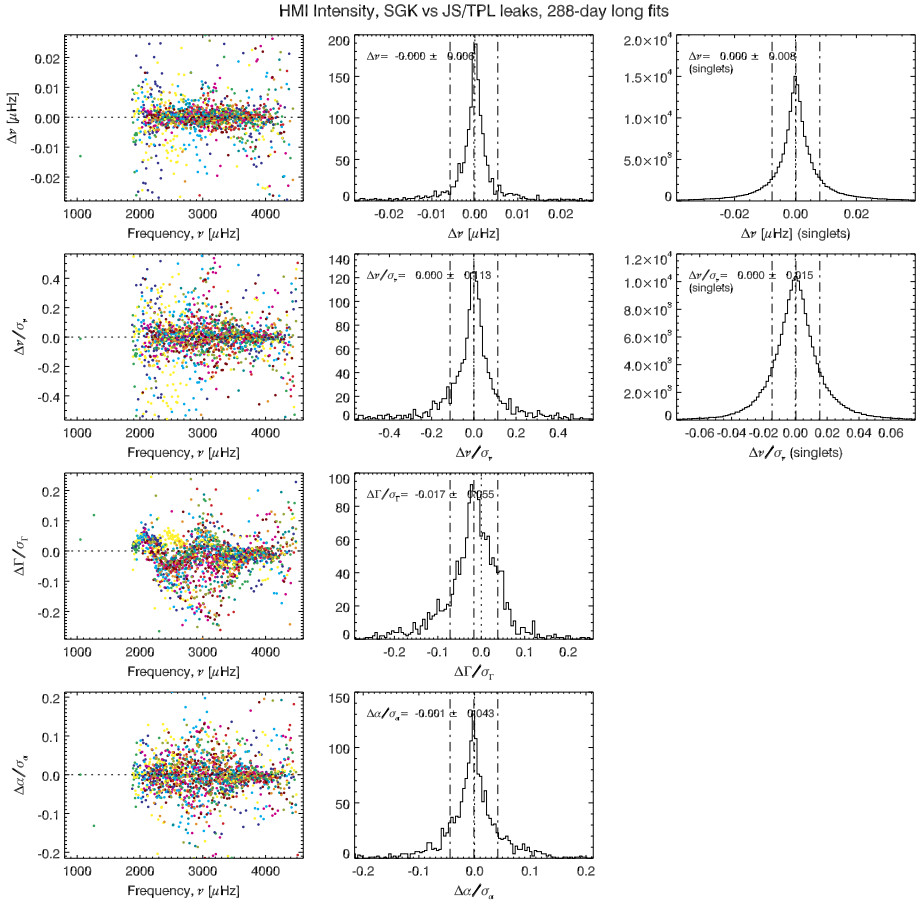

Figure 17 Comparison of mode characteristics derived from fitting a 288-day long time series after converting singlets to multiplets, and for singlets, using two different leakage-matrix computations, namely mine based on $I(\mu)$ and the one computed by the Stanford group. As for Figure 16, the *panels* show from top to bottom the raw and scaled frequency differences for multiplets and singlets, and the FWHM and asymmetry scaled differences. The *panels in the leftmost column* show the multiplet differences with colors corresponding to the mode orders $[n]$. The *panels in the middle column* show the histogram distribution of the differences for the multiplets, while the *panels in the rightmost column* show the histogram distribution of the differences computed using singlets. *Vertical lines* are drawn at zero and at the mean plus or minus one standard deviation around the mean. The resulting bias and spread remain small. Again, the FWHM differences show a non-negligible bias, which, while small, shows a hint of systematic distribution with order and frequency.

3. Conclusions

Initial results from fitting HMI intensity observations using my fitting method and including the mode-profile asymmetry show a remarkable agreement of the derived mode characteristics with the corresponding values derived from coeval velocity observations. Of course, the mode asymmetry for the intensity is of opposite sign to the mode asymmetry for the velocity, as anticipated, and it is also larger in magnitude. The comparison of mode frequency and FWHM determinations based on intensity and velocity shows no bias with a uniform normal distribution. The RMS of $\Delta\nu/\sigma_\nu$ is around 0.3 for singlets and around 0.9 to 1.1 for

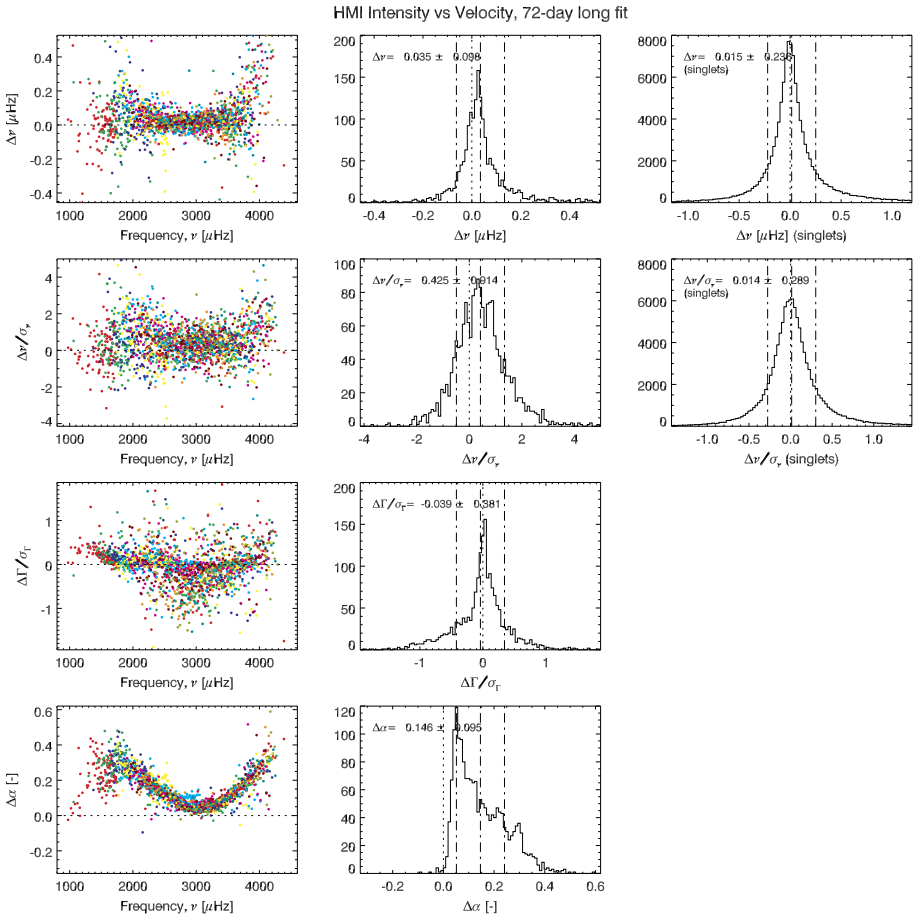

Figure 18 Comparison of mode characteristics derived from fitting a 72-day long time series after converting singlets to multiplets, and for singlets, resulting from fitting coeval intensity and velocity time series. As for Figures 16 and 17, the *panels* show from top to bottom the raw and scaled frequency differences for multiplets and singlets, and the FWHM and asymmetry scaled differences. The *panels in the leftmost column* show the multiplet differences, with colors corresponding to the mode orders $[n]$. The *panels in the middle column* show the histogram distribution of the differences for the multiplets, while the *panels in the rightmost column* show the histogram distribution of the differences computed using singlets. *Vertical lines* are drawn at zero and at the mean plus or minus one standard deviation around the mean. The means and standard deviation of the differences are negligible for frequencies $[\nu]$ and FWHM $[\Gamma]$. As expected, the differences in asymmetries are large and show a clear and smooth dependence on frequency.

multiplets. The RMS of $\Delta\Gamma/\sigma_\Gamma$ is around 0.4 to 0.5 (see Table 3). Results from mode fitting using either velocity or intensity observations show a different coverage in ℓ–ν but a very similar precision on the mode frequency. This being said, my attempt to validate various estimates of the leakage matrix for intensity shows residual inconsistencies that need to be resolved. I also showed that despite these inconsistencies, the derived modes' characteristics do not seem to be affected in any systematic way, at least for the precision resulting from fitting 72-day or 288-day long time series. Fitting a much longer time series may indicate systematic errors associated with the leakage-matrix determination.

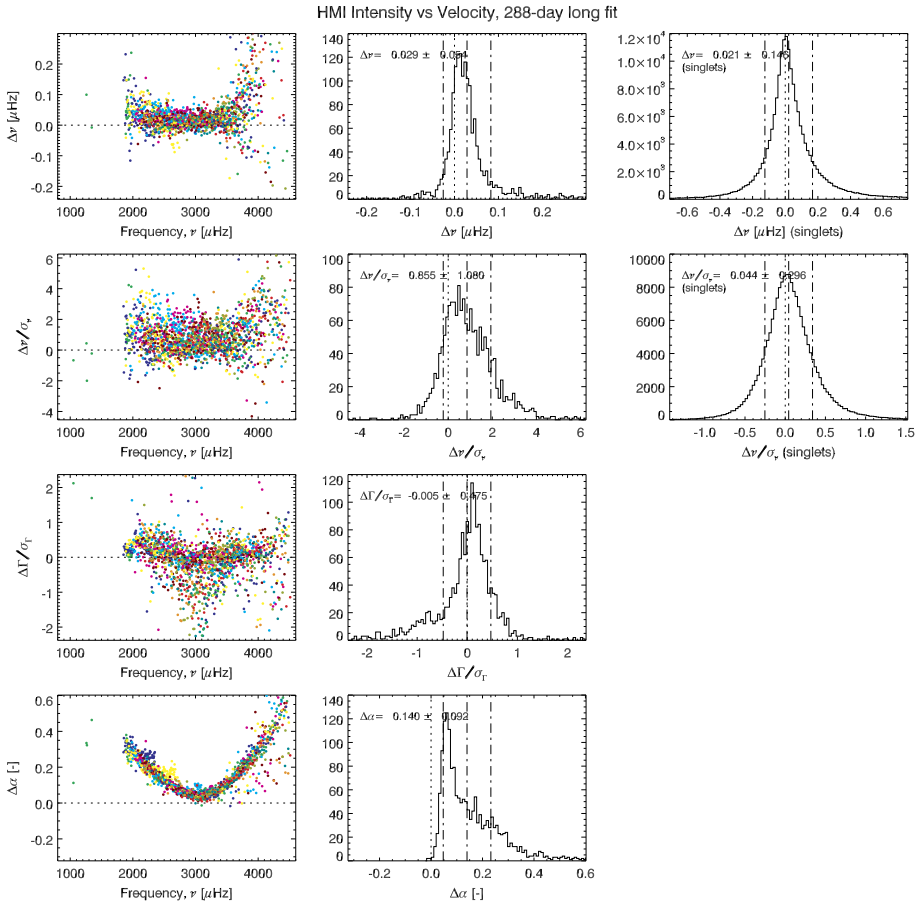

Figure 19 Comparison of mode characteristics derived from fitting a 288-day long time series after converting singlets to multiplets, and for singlets, resulting from fitting coeval intensity and velocity time series. As for Figures 16 to 18, the *panels* show from top to bottom the raw and scaled frequency differences for multiplets and singlets, and the FWHM and asymmetry scaled differences. The *panels in the leftmost column* show the multiplet differences, with colors corresponding to the mode orders [n]. The *panels in the middle column* show the histogram distribution of the differences for the multiplets, while the *panels in the rightmost column* show the histogram distribution of the differences computed using singlets. *Vertical lines* are drawn at zero and at the mean plus or minus one standard deviation around the mean. Similarly to the 72-day long case, the differences in asymmetries are large and show a clear and smooth dependence on frequency.

One of the main drawbacks of intensity observations is the much higher noise level at low frequencies than in velocity observations. For reasons that I have yet to understand and that therefore warrant more work, my fitting method was able to determine low-order, low-frequency singlets for the shorter time series, but not for the longer series. One simple explanation could be that the sanity rejection is not stringent enough and the fitted modes are just realization noise spikes that happened to coincide with a mode frequency and should be ignored. The principle that I have followed, namely to fit time series of different lengths, again proves to be a good idea. I expect to fit additional HMI intensity data as they become available and fit them using the factor of two length progression that I have used for the

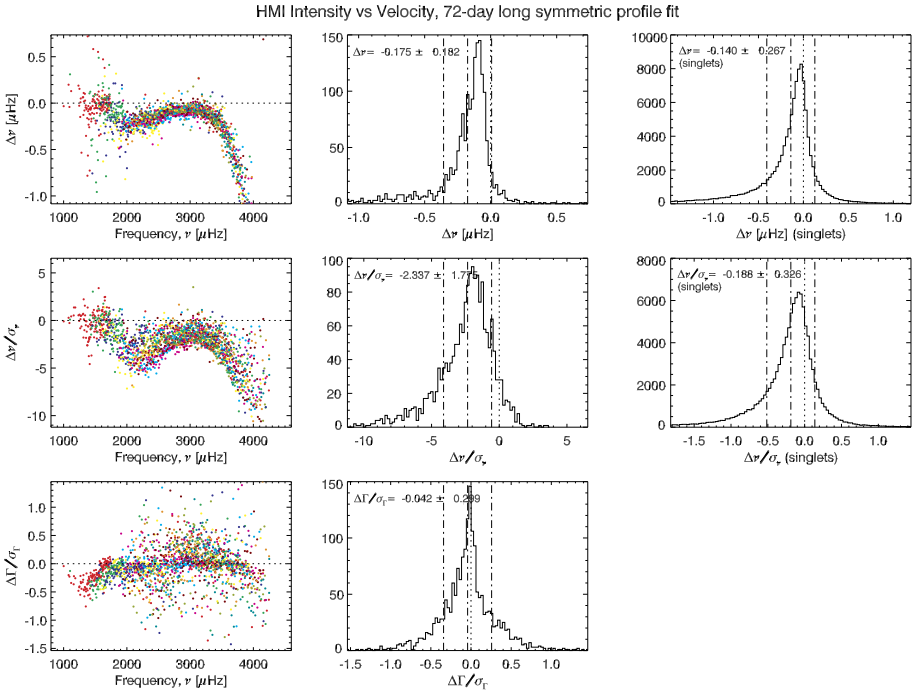

Figure 20 Comparison of mode characteristics derived from fitting a 72-day long time series after converting singlets to multiplets, and for singlets, resulting from fitting coeval intensity and velocity time series, using in both cases a symmetric peak profile [$\alpha_{n,\ell} = 0$]. As for Figures 16 to 19, the *panels* show from top to bottom the raw and scaled frequency differences for multiplets and singlets, and the scaled differences of the FWHM. The *panels in the leftmost column* show the multiplet differences, with colors corresponding to the mode orders [n]. The *panels in the middle column* show the histogram distribution of the differences for the multiplets, while the *panels in the rightmost column* show the histogram distribution of the differences computed using singlets. *Vertical lines* are drawn at zero and at the mean plus or minus one standard deviation around the mean. The frequency differences become significant and systematic when ignoring the mode-profile asymmetry.

velocity observations, namely fitting time series of 36 days, 72 days, 144 days, 288 days, *etc.*

Finally, comparisons of mode characteristics derived by fitting a symmetric mode profile show unequivocally that the systematic bias is introduced in the mode-frequency determinations by ignoring the asymmetry. Furthermore, by fitting additional HMI intensity observations that will cover most of Cycle 24, I will be able to confirm whether the mode asymmetry for both intensity and velocity changes with solar activity. I see these changes in my fitting of velocity observations, but they are not seen by others. Indeed, coeval intensity- and velocity-derived frequencies ought to agree consistently, independently of the solar-activity level. Therefore, a change in the velocity-derived asymmetry will have to be matched by a change in the intensity-derived asymmetry, although of opposite sign and different in magnitude, to maintain agreement of the derived frequencies.

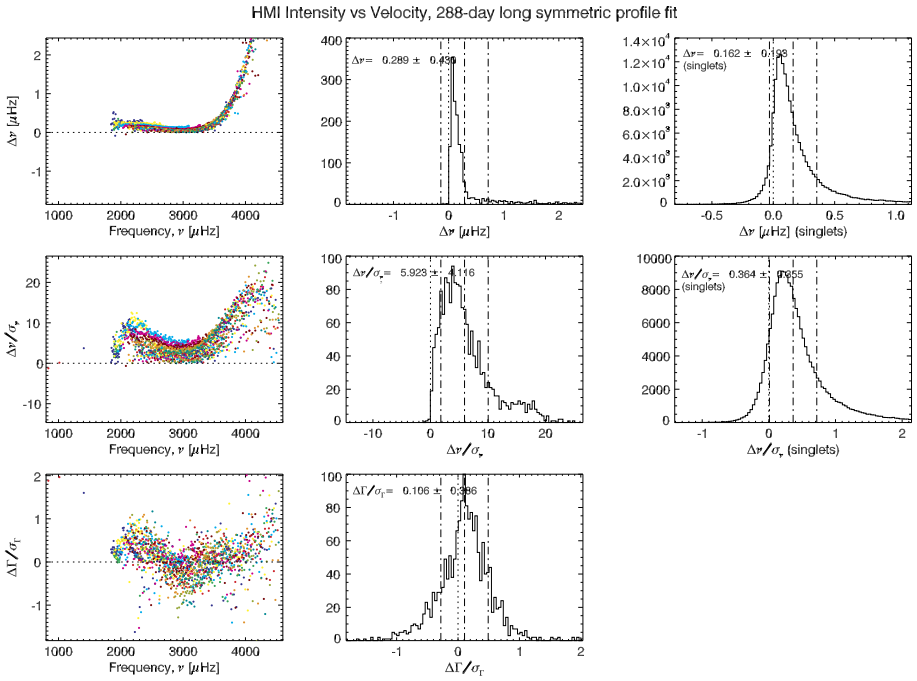

Figure 21 Comparison of mode characteristics derived from fitting a 288-day long time series after converting singlets into multiplets, and for singlets, resulting from fitting coeval intensity and velocity time series, using in both cases a symmetric peak profile $[\alpha_{n,\ell} = 0]$. As for Figures 16 to 20, the *panels* show from top to bottom the raw and scaled frequency differences for multiplets and singlets, and the scaled differences of the FWHM. The *panels in the leftmost column* show the multiplet differences, with colors corresponding to the mode orders $[n]$. The *panels in the middle column* show the histogram distribution of the differences for the multiplets, while the *panels in the rightmost column* show the histogram distribution of the differences computed using singlets. *Vertical lines* are drawn at zero and at the mean plus or minus one standard deviation around the mean. The frequency differences are quite significant and systematic when ignoring the mode-profile asymmetry.

Acknowledgements HMI data are courtesy of NASA/SDO and the HMI science team; HMI is supported by NASA contract NAS5–02139 to Stanford University. The author wishes to thank T.P. Larson and J. Schou for providing their estimate of the intensity leakage matrix. The author is supported by NASA grant NNX15AL65G. Most of the computations done for this work were carried out on the Smithsonian Institution's High Performance Cluster (*SI/HPC*).

Disclosure of Potential Conflicts of Interest The author declares that he has no conflicts of interest.

References

Barban, C., Hill, F., Kras, S.: 2004, Simultaneous velocity-intensity spectral and cross-spectral fitting of helioseismic data. *Astrophys. J.* **602**, 516. DOI. ADS.

Corbard, T., Salabert, D., Boumier, P., Picard Team: 2013, Helioseismology from SODISM and HMI intensity images. In: Jain, K., Tripathy, S.C., Hill, F., Leibacher, J.W., Pevtsov, A.A. (eds.) *Fifty Years of Seismology of the Sun and Stars* **CS-478**, Astron. Soc. Pacific, San Francisco, 151. ADS.

Couvidat, S., Schou, J., Shine, R.A., Bush, R.I., Miles, J.W., Scherrer, P.H., Rairden, R.L.: 2012, Wavelength dependence of the Helioseismic and Magnetic Imager (HMI) instrument onboard the Solar Dynamics Observatory (SDO). *Solar Phys.* **275**, 285. DOI. ADS.

Couvidat, S., Schou, J., Hoeksema, J.T., Bogart, R.S., Bush, R.I., Duvall, T.L., Liu, Y., Norton, A.A., Scherrer, P.H.: 2016, Observables processing for the Helioseismic and Magnetic Imager instrument on the Solar Dynamics Observatory. *Solar Phys.* **291**, 1887. DOI. ADS.

Duvall, T.L. Jr., Jefferies, S.M., Harvey, J.W., Osaki, Y., Pomerantz, M.A.: 1993, Asymmetries of solar oscillation line profiles. *Astrophys. J.* **410**, 829. DOI. ADS.

Froehlich, C., Andersen, B.N., Berthomieu, G., Crommelynck, D., Delache, P., Domingo, V., Jimenez, A., Jones, A.R., Roca Cortés, T., Wehrli, C.: 1988, VIRGO: The solar monitor experiment on SOHO. In: Rolfe, E.J. (ed.) *Seismology of the Sun and Sun-Like Stars*, **SP-286**, ESA, Noordwijk, 371. ADS.

Frohlich, C., Andersen, B.N., Appourchaux, T., Berthomieu, G., Crommelynck, D.A., Domingo, V., Fichot, A., Finsterle, W., Gomez, M.F., Gough, D., Jimenez, A., Leifsen, T., Lombaerts, M., Pap, J.M., Provost, J., Cortes, T.R., Romero, J., Roth, H., Sekii, T., Telljohann, U., Toutain, T., Wehrli, C.: 1997, First results from VIRGO, the experiment for helioseismology and solar irradiance monitoring on SOHO. *Solar Phys.* **170**, 1. DOI. ADS.

Komm, R., Howe, R., Hill, F.: 2002, Localizing width and energy of solar global p-modes. *Astrophys. J.* **572**, 663. DOI. ADS.

Korzennik, S.G.: 2005, A mode-fitting methodology optimized for very long helioseismic time series. *Astrophys. J.* **626**, 585. DOI. ADS.

Korzennik, S.G.: 2008, YAOPBM−II: Extension to higher degrees and to shorter time series. *J. Phys.* **CS-118**, 012082. DOI. ADS.

Korzennik, S.G.: 2013, Mode frequencies from GONG, MDI, and HMI data. In: Jain, K., Tripathy, S.C., Hill, F., Leibacher, J.W., Pevtsov, A.A. (eds.) *Fifty Years of Seismology of the Sun and Stars* **CS-478**, Astron. Soc. Pacific, San Francisco, 137. ADS.

Korzennik, S.G., Rabello-Soares, M.C., Schou, J.: 2004, On the determination of Michelson Doppler Imager high-degree mode frequencies. *Astrophys. J.* **602**, 481. DOI. ADS.

Oliviero, M., Severino, G., Straus, T.: 2001, A high frequency and high *l* resolution intensity-velocity phase differences from GONG data. In: Wilson, A., Pallé, P.L. (eds.) *SOHO 10/GONG 2000 Workshop: Helio- and Asteroseismology at the Dawn of the Millennium* **SP-464**, ESA, Noordwijk,669. ADS.

Pierce, A.K., Slaughter, C.D.: 1977, Solar limb darkening, I: At wavelengths of 3033-7297. *Solar Phys.* **51**, 25. DOI. ADS.

Salabert, D., García, R.A., Jiménez, A.: 2013, Differences of the solar magnetic activity signature in velocity and intensity helioseismic observations. In: Jain, K., Tripathy, S.C., Hill, F., Leibacher, J.W., Pevtsov, A.A. (eds.) *Fifty Years of Seismology of the Sun and Stars* **CS-478**, Astron. Soc. Pacific, San Francisco, 145. ADS.

Schou, J.: 1999, Migration of zonal flows detected using Michelson Doppler Imager F-mode frequency splittings. *Astrophys. J. Lett.* **523**, L181. DOI. ADS.

Schou, J., Scherrer, P.H., Bush, R.I., Wachter, R., Couvidat, S., Rabello-Soares, M.C., Bogart, R.S., Hoeksema, J.T., Liu, Y., Duvall, T.L., Akin, D.J., Allard, B.A., Miles, J.W., Rairden, R., Shine, R.A., Tarbell, T.D., Title, A.M., Wolfson, C.J., Elmore, D.F., Norton, A.A., Tomczyk, S.: 2012, Design and ground calibration of the Helioseismic and Magnetic Imager (HMI) instrument on the Solar Dynamics Observatory (SDO). *Solar Phys.* **275**, 229. DOI. ADS.

Woodard, M.F.: 1984, Short-period oscillations in the total solar irradiance. PhD thesis, University of California, San Diego. ADS.